

# MOOSE-based Tritium Migration Analysis Program, Version 8 (TMAP8) for advanced open-source tritium transport and fuel cycle modeling

Pierre-Clément A. Simon<sup>a,b</sup>, Casey T. Icenhour<sup>a</sup>, Gyanender Singh<sup>a</sup>, Alexander D. Lindsay<sup>a</sup>, Chaitanya Bhawe<sup>a</sup>, Lin Yang<sup>a</sup>, Adriaan Riet<sup>a</sup>, Yifeng Che<sup>a,d</sup>, Paul Humrickhouse<sup>c</sup>, Patrick Calderoni<sup>a</sup>, Masashi Shimada<sup>a</sup>

<sup>a</sup> Idaho National Laboratory, Idaho Falls, ID, 83415, USA

<sup>b</sup> The Ken and Mary Alice Lindquist Department of Nuclear Engineering, The Pennsylvania State University, University Park, PA, 16802, USA

<sup>c</sup> Oak Ridge National Laboratory, Oak Ridge, TN, 37830, USA

<sup>d</sup> Woodruff School of Mechanical Engineering, Georgia Institute of Technology, Atlanta, GA 30332, USA

## ARTICLE INFO

Dataset link: <https://github.com/idaholab/TMAP8>, <https://mooseframework.inl.gov/TMAP8/index.html>, <https://github.com/idaholab/FENIX>, <https://mooseframework.inl.gov/fenix/>

### Keywords:

TMAP  
Tritium transport and fuel cycle  
Computational fusion  
Verification and validation  
Software quality assurance  
MOOSE

## ABSTRACT

Tritium management is critical for the safety, sustainability, and economics of fusion energy systems, and advanced and reliable modeling tools help accelerate the development of tritium technologies. This paper presents the Tritium Migration Analysis Program, Version 8 (TMAP8), an open-source, MOOSE-based application developed to provide state-of-the-art tritium transport and fuel cycle modeling capabilities. TMAP8 aims to expand the capabilities of previous versions (i.e., TMAP4 and TMAP7) by leveraging modern computational techniques, ensuring high software quality assurance standards (key to building trust), and enabling multispecies, multiscale, and multiphysics simulations for integrated tritium transport modeling in complex geometries. This paper outlines TMAP8's scope and rigorous development practices, emphasizing its transparency, accessibility, modularity, and reliability. We present the current suite of verification and validation cases based on those from TMAP4, demonstrating TMAP8's accuracy and reliability against analytical solutions and experimental data. Additionally, the paper showcases TMAP8's integrated fuel cycle modeling capabilities, highlighting its applicability at various scales and levels. The TMAP8 code and documentation are openly available, promoting collaborative development and widespread adoption within the fusion community. Future work will soon expand TMAP8's verification and validation suite to include those from TMAP7 and other recent experimental studies for validation.

## 1. Introduction

Tracking tritium inventory is of primary importance in fusion energy systems for several reasons. As a radioactive hydrogen isotope, tracking tritium is one of the main focuses of fusion safety assessments [1]. Moreover, since tritium decays with a half-life of  $\approx 12.32$  years and is not found abundantly on earth, it must be bred to sustain a fusion energy system [2]. Early on, the need for reliable, accurate modeling and simulation tools to perform safety assessments, interpret experimental results, and perform design studies became evident, and the Fusion Safety Program at Idaho National Laboratory (INL) consequently developed the tritium migration analysis program (TMAP). Since then, several versions of TMAP have been released. TMAP4 was published in 1992, and TMAP7 followed in 2006 [3–7].

TMAP4 enabled tritium permeation and heat conduction modeling in one-dimensional (1D) domains with one trapping site population and

zero-dimensional (0D) fluid transport at interfaces and boundaries [5, 6]. TMAP7 expanded these capabilities by enabling three different trapping site populations to be modeled (instead of one), increasing the accuracy of surface kinetics calculations and supporting heteronuclear and homonuclear molecule formation [7,8]. TMAP4 and TMAP7 have been extensively used. Examples include fusion safety studies of ITER and modeling of tritium production and permeation, amongst others [9]. These tools, however, have significant limitations in that (a) they offer limited modeling capabilities (e.g., a maximum of three trapping site populations and no pathway toward high-fidelity multiphysics simulations or multidimensional systems), (b) they cannot leverage modern computing facilities, (c) their users can no longer rely on active development and support, and (d) these tools are export controlled.

To alleviate these limitations and address the modeling needs of the growing fusion industry, INL is developing a new version of TMAP

\* Corresponding author.

E-mail address: [pierreclément.simon@inl.gov](mailto:pierreclément.simon@inl.gov) (P.-C.A. Simon).

<https://doi.org/10.1016/j.fusengdes.2025.114874>

Received 12 December 2024; Received in revised form 2 February 2025; Accepted 11 February 2025

Available online 27 February 2025

0920-3796/© 2025 The Authors. Published by Elsevier B.V. This is an open access article under the CC BY license (<http://creativecommons.org/licenses/by/4.0/>).

based on the Multiphysics Object Oriented Simulation Environment (MOOSE) framework: TMAP8 [10–12]. MOOSE is an open source framework developed primarily by INL with contributions from many institutions worldwide [13]. MOOSE has several attributes that make it a very powerful tool for the rapid development of energy systems. On a technical level, (1) it was designed to perform complex multiphysics simulation on one integrated platform with in-memory coupling, (2) it enables massively parallel simulations on thousands of cores [13], (3) it is modular and supports agile, concurrent development, and (4) it is dimension agnostic, meaning that it supports 0D, 1D, two-dimensional (2D), and three-dimensional (3D) simulations without additional code development. It has also been demonstrated to enable simulations on computer-aided design (often called CAD) geometries, and can therefore model complex fusion geometries [14]. Moreover, MOOSE is open source and follows high software quality assurance (SQA) standards. This openness increases its availability, transparency, and reach, while the high SQA standards ensure its reliability. MOOSE, supported by the United States Department of Energy (DOE) Office of Nuclear Energy's Nuclear Energy Advanced Modeling and Simulation (NEAMS) Program, has been successfully applied in the fission energy space where it enables many MOOSE-based applications [15–23]. MOOSE is currently being leveraged in the fusion energy space [24–27], and TMAP8 is one of the products of this effort [10–12].

TMAP8, as a MOOSE-based tool, inherits these advantageous attributes to provide open-source and reliable state-of-the-art tritium modeling capabilities—beyond what TMAP4 and TMAP7 could enable. This paper serves as a general introduction to TMAP8. In Section 2, we discuss TMAP8's scope, its rigorous software development practices, and the SQA standards that it follows to be Nuclear Quality Assurance, Level 1 (NQA-1) standard compliant, all in the context of other available tritium modeling tools. In Section 3 and later in Section 4, we describe the verification and validation (V&V) cases, respectively, available in TMAP8. These cases demonstrate that TMAP8 is a capable and reliable tritium and heat conduction modeling and simulation tool. In Section 5, we describe TMAP8's fuel cycle modeling capabilities, highlighting TMAP8's ability to model tritium transport at many levels. We conclude the paper and describe ongoing and future work in Section 6. The Data Availability section provides links to TMAP8's open-source base code and documentation.

## 2. Overview of TMAP8's scope, development approach, and software quality assurance

### 2.1. TMAP8's scope

TMAP4 and TMAP7 are well-established component-level codes, and TMAP8 first aims to match their capabilities and demonstrate that it can accurately model the same cases [6,7]. However, since TMAP8 inherits MOOSE's features, TMAP8's scope and abilities go well beyond TMAP4's and TMAP7's. This subsection describes this scope in the context of other existing tritium modeling tools.

Tritium modeling codes are often divided into two categories: component-level and system-level codes [28]. A non-exhaustive list of component-level codes includes TMAP4 [3,6], TMAP7 [4,7], TESSIM-X [29], FESTIM [30,31], Achlys (a MOOSE-based tool from the United Kingdom Atomic Energy Authority) [32], BISON (also a MOOSE-based tool, but commonly used for fuel performance) [15,33], the TRIMO code presented in Ref. [34], and several applications based on COMSOL multiphysics or other commercial codes (mHIT [35], Aspen HYSYS [36], CFTSIM [37] and the code presented in Ref. [38]). System-level codes include FUS TPC [39], SAM (another MOOSE-based application) [23,40], and others such as ModAn and the EcosimPro-based code mentioned in Ref. [28]. As discussed in Ref. [28], some of these tools, while focusing in one area, tend to offer capabilities at different levels. Since MOOSE has a proven record in enabling multiscale modeling [41,42], TMAP8 is being developed as a multiscale tool capable of

performing simulations from the pore microstructure scale (which has been demonstrated in [11]), to the component scale (see Sections 3 and 4), and up to the system level (see Section 5). Moreover, the MOOSE MultiApp system enables concurrent simulations at different scales with in-memory exchanges of information between scales [41], which will be utilized in TMAP8. Furthermore, TMAP8 enables 0D, 1D, 2D, and 3D simulations, providing an unparalleled level of flexibility for users to select the appropriate balance of computational cost and fidelity depending on their needs. This flexibility is enhanced by the ability to develop CAD-based workflows, hence enabling simulations on complex fusion geometries [14].

In addition, TMAP8 can easily be coupled to other MOOSE physics modules or MOOSE-based applications, enabling high fidelity coupled simulations that account for irradiation, material behavior evolution, and thermomechanics, etc. This differentiates TMAP8 from TMAP4, TMAP7, and other tritium modeling tools that are focused on a single physics and do not permit easy coupling with other capabilities without utilization of third-party data-handling frameworks. Recently, TMAP8 was added to the MOOSE-based Fusion ENergy Integrated multiphys-X (FENIX) application, which is a fully integrated multiphysics application designed to perform high fidelity modeling of fusion systems [24,43]. Since these applications are built on the same framework, coupling is done in memory, and users can seamlessly transition from one tool to another without hurdles [24]. Moreover, TMAP8 can accommodate the high computational needs sometimes required by high fidelity simulations thanks to its inheritance of MOOSE's massive parallel capabilities [13], which enable users to run TMAP8 on a laptop or on high-performing computer systems depending on the simulation's requirements.

Beyond coupling with other physics modules and MOOSE-based applications, TMAP8 inherits the stochastic tools module (STM) from MOOSE [44]. The STM is under constant development but already enables parameter study, sensitivity analysis, parameter calibration, surrogate modeling, uncertainty quantification (UQ) (including Bayesian inference), and deep reinforcement learning. The STM is optimized to run analyses on MOOSE-based simulations with high performance, and some of the basic functionalities are demonstrated in Section 4 to show how TMAP8 can leverage it to enhance its predictions. The fact that TMAP8 can utilize these stochastic capabilities is crucial for effective and quantitative safety assessment and uncertainty studies.

Furthermore, TMAP8 makes these capabilities available to all by being open source and available on the widely-used GitHub code repository platform [10]. Export controlled, commercial, and internal codes can be challenging, costly, or even impossible to access and use. By developing TMAP8 as an open-source code, we aim to (1) enable wide-ranging collaborations and partnerships to accelerate development and increase adoption, (2) promote transparency and openness to build trust and understanding, and (3) provide access to advanced modeling and simulation tools to all to support the rapid development of the future fusion workforce and industry. The fact that TMAP8 is open-source, however, does not prevent collaborators from extending TMAP8 with custom in-house capabilities. Since TMAP8 is developed under the Lesser General Public License, version 2.1, applications can be built on top of TMAP8 without being released as open source. This is key to the adoption of TMAP8 by other institutions, in particular private partners.

TMAP8 also aims to reproduce and extend the extensive suite of V&V cases from TMAP4 and TMAP7. Verification is the process of ensuring that a computational model accurately represents the underlying mathematical model and its solution. Verification can be satisfied by comparing modeling predictions against analytical solutions for simple cases, or leveraging the method of manufactured solutions (MMS) [45], which is supported in MOOSE. Validation, on the other hand, is the process of determining the extent to which a model accurately represents the real world for its intended uses, which requires comparison against experimental data [46]. By making this list available to all with online documentation that is automatically generated on the fly

with the latest simulation results (also available at Ref. [10]), we aim to increase transparency and reproducibility compared to the well-respected V&V suite from TMAP4 and TMAP7. The updated list of V&V cases is available at Ref. [10] on the TMAP8 website, and the cases corresponding to the TMAP4 V&V suite are reproduced in Sections 3 and 4 [6]. This focus on V&V is aligned with the high SQA standards being followed throughout TMAP8's development (see Section 2.2). This emphasis on software quality is one of the key attributes of TMAP8, making it uniquely poised for reliable safety assessments and design analyses.

In summary, TMAP8 offers open source capabilities that extend well beyond TMAP4 and TMAP7. TMAP8 is developed to address some of the crucial needs of the fusion and fission industry related to high fidelity tritium transport modeling at multiple scales with an emphasis on openness, reproducibility, high software quality, and flexibility for future expansions.

## 2.2. Software development practices and software quality assurance

Given the fast pace of fusion science & technology (FS&T) development, research institutions and private industry require trusted, comprehensive, and flexible modeling and simulation tools in order to close FS&T technology gaps and prepare a fusion workforce that is ready and able to develop commercial pilot plants. Trust is earned through comprehensive V&V practices (the initial efforts of which in TMAP8 are documented in Sections 3 and 4), but V&V alone is not enough. Software products integral to the design, engineering, licensure, and safe operation of fusion power plants need to demonstrate stability, thorough planning, and high quality execution to properly support FS&T development.

Given its basis on the MOOSE framework, TMAP8 seeks to follow the same high standard of software quality [47]. MOOSE and other MOOSE-based applications, such as BISON, the nuclear fission fuel performance code [15], use an agile, continuous integration development process. MOOSE and BISON have been independently audited to meet the software quality standards as defined by the NQA-1 standard [48]. TMAP8 itself has not been through a formal independent audit against the NQA-1 standard as of this writing, but follows the same guidelines and procedures as MOOSE and BISON. Such an audit will be undertaken in the future. NQA-1 describes what must be satisfied in order for an organization to supply an item (such as software) to operate in a safety function within a nuclear facility. While fusion currently has different standardized practices from fission, adherence to NQA-1 could allow third-party fusion industry collaborators or eventual regulatory bodies to trust that the design and performance of a system is sound and as-intended to meet the safety and operational goals of the industry and wider community. Establishing and executing a quality process on a software product for formal acceptance by a regulatory body (also known as a Commercial Grade Dedication) usually involves significant investment in time and resources to provide the evidence and paperwork necessary. The MOOSE ecosystem (and therefore TMAP8) provides ready-made infrastructure to facilitate compliance by the industry end-user with the standard, supported by the MOOSE project itself: (1) the MOOSE TestHarness, (2) the continuous integration, verification, enhancement, and testing (CIVET) system, and (3) the MooseDocs documentation system.

These three components support various aspects of TMAP8's NQA-1 compliance. The TestHarness provides local testing and connectivity of software requirements, design documents, V&V, and test configuration for individual test cases. CIVET utilizes the TestHarness, alongside its own "recipes", for testing various system configurations (across multiple operations systems, architectures, and software stacks). CIVET and well-designed, requirements-driven tests add robustness to the project. MooseDocs can utilize the metadata provided by the TestHarness to create in-depth documentation (e.g., web pages, presentations, and reports) for day-to-day use by users and developers (e.g., tutorials,

object documentation, and usage guides) as well as for SQA compliance (e.g., software test plans, V&V reports, and software requirements specifications). CIVET can also facilitate the on-the-fly generation of MooseDocs output for use in the ongoing development of new features (in the context of code pull requests [PRs] or merge requests [MRs]) and for regular posting to a common public-facing website [10].

The available software infrastructure in TMAP8 is only one component of facilitating high SQA and development standards. For TMAP8 developers, the other component focuses on the code submission and integration process. PRs (as referred to by the GitHub code repository system on which TMAP8 is stored) and MRs (as referred to by GitLab) refer to the submission of a piece of modified or newly developed code for merging and inclusion within a software project. We will refer to these as PRs for the remainder of this document. The creation of a TMAP8 PR must derive from a new software requirement, adjusted requirement, or discovered deficiency; an issue ticket is then expected to be created to allow the code developer to engage with the TMAP8 community and change control board (CCB) on design considerations and paths forward. When a PR is created on the TMAP8 GitHub repository, code changes are connected back to the driving issue, fostering transparency and traceability. All new or modified capability must be tested (TMAP8 currently has a total code line coverage rate of over 91%) and tied to a formal software requirement and design documentation. This is then checked by the CIVET system and tested across a plurality of platforms and architectures across the Linux and MacOS ecosystems; CIVET then reports a pass/fail status back to the PR interface for evaluation by a CCB reviewer. Independent review is next in the process: a CCB member (a seasoned, appropriately trained, and approved member of the development team who has write-permissions to TMAP8) reviews the PR, checking it for code style adherence, test quality, documentation quality, and general adherence to the TMAP8 software quality assurance plan. If, after passing all tests and independent review, the PR is ready to be merged in, a TMAP8 CCB member will merge it into the code development branch. CIVET will then perform further testing on the integrated code before merging it into the release-candidate or "production" branch. The combination of automated infrastructure, continuous testing, and independent review procedures ensures stable development, with the capacity to respond in an agile fashion if something were to go awry or a bug were to be discovered.

A common misconception is that robust SQA practices hinder rapid code development. Effective SQA practices with automated, continuous testing, such as the ones deployed in MOOSE and TMAP8, accelerate development in the long run by facilitating early detection of issues, providing a structured and transparent way to obtain consensus on new code, reducing technical debt and re-work thanks to increased code quality, and increasing documentation.

As previously mentioned, regulatory and licensing compliance is a significant strength of this approach. There have been several examples of successful application of this process in the MOOSE-based application ecosystem; one that we will focus on to close this section is the Kairos Power (KP)-developed KP-BISON application [49]. KP-BISON is based on the BISON code and models the fuel performance of tristructural isotropic (TRISO) fuel for Kairos's specific application. Kairos developed KP-BISON as an extension to the main BISON application, but utilized the software development practices described here to develop and refine their model code, submit bugfixes and new features to the BISON application, and develop their SQA paperwork for submission to the United States (U.S.) Nuclear Regulatory Commission, which is currently evaluating Kairos's fuel and fission reactor technology for an operational license [50]. While licensing and regulation for fusion is still in a state of flux in the domestic U.S. and internationally, TMAP8's approach can provide a trusted application design and engineering that is compatible with the aims of high operational performance and safety.

### 2.3. The finite element method

TMAP8 uses the finite element method implemented in MOOSE to solve the partial differential equations (PDEs) governing tritium transport. In this section, we aim to provide a highlight of how TMAP8 solves coupled equations such as the diffusion and trapping equations. Readers interested in more general and more in-depth descriptions are encouraged to refer to Refs. [51,52] or other related textbooks.

TMAP8 solves diffusion and trapping together in a tightly coupled fashion (with no operator splitting). The first step is to derive the governing equations representing the model to be used. Once the governing equations are derived, they need to be converted to their weak form. An example of this process for coupled diffusion and trapping with three trapping sites is available in Appendix. In general terms, deriving the weak form of PDEs consist in first developing an integral form of the PDEs governing the desired physics. This is also known as a “weighted residual” form, weakly satisfying the original equations with respect to the finite element test/basis functions. By default, we use a continuous Galerkin formulation, which assumes that the test and basis functions are one-and-the-same. After deriving this so-called “weak form”, the equations are represented by sums of integral terms, each of which is represented in TMAP8/MOOSE as an individual “kernel”. Arbitrary combinations of kernels can represent a myriad of different mathematical forms that represent the physics of interest. Each kernel contributes to the numerical system’s residual matrix, which in turn influences the construction of the Jacobian matrix used in the Newton or Newton–Krylov based solver configurations. The actual solver being used dictates if, and with how much accuracy, the Jacobian terms are computed. The solvers available in MOOSE/TMAP8 include:

- The Newton solver, which provides a direct solution of the system of equations using Newton’s method. The full and accurate Jacobian is required. The user must also select a preconditioner for systems with multiple nonlinear variables.
- The Jacobian-free Newton–Krylov (JFNK) solver, for which no Jacobian terms are needed. However, JFNK usually does not perform well without preconditioning.
- The preconditioned JFNK (PJFNK) solver, for which the Jacobian is used to precondition the matrix, but it does not have to be fully correct and can neglect off-diagonal terms. This solver often appropriately balances accuracy and costs for tritium transport applications.
- The finite difference solver, which uses finite difference to compute the Jacobian. This approach is more expensive and less accurate than alternatives and should be use for testing purposes
- The linear solver, mostly applicable to linear systems, or when computational costs need to be minimized.

Several preconditioners are available, with varying degrees of accuracy and computational costs. An exhaustive list of capabilities is available on the MOOSE framework documentation website. Note that as finite volume capabilities become more widely available in MOOSE, TMAP8 will be able to utilize these capabilities whenever relevant.

### 3. Verification of TMAP8

As stated above, verification is the process of determining that a computational model accurately represents the underlying mathematical model and its solution [46]. To adhere to our strict SQA standards and prove that TMAP8 is reliable and trustworthy, we verify TMAP8’s capabilities in conditions relevant to tritium transport. To that end, we utilize the extensive V&V suite proposed in Refs. [6–8], which covers important physics required for tritium transport and heat conduction. In this section, we describe how TMAP8 is currently verified at the same level as TMAP4 (i.e., from ver-1a to ver-1h) [6]. Ref. [7] proposes additional verification cases for TMAP7, which will be the focus of future work. Note, however, that whenever Ref. [7] (TMAP7) updated

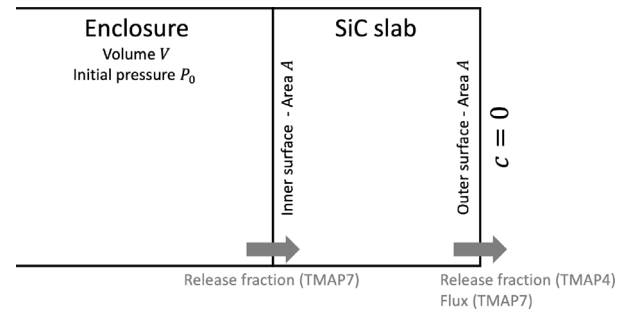


Fig. 1. Schematic of the ver-1a case and illustration of the quantities used for verification.

an existing case from Ref. [6] (TMAP4) with a different metric for verification, different model parameters, or any other small change, we have reproduced both the original case from Ref. [6] and the updated case from Ref. [7]. We also extend the verification suite by introducing verification by MMS [45], which is supported by MOOSE and TMAP8. The MMS approach is especially powerful when the case is too complex to derive an analytical solution. We apply it below to a case coupling species diffusion and multiple trapping. The input files and scripts to reproduce the results and the figures below are available at Ref. [10] and in the online TMAP8 documentation.

#### 3.1. Ver-1a: Depleting source problem

##### 3.1.1. General case description

This verification case consists of an enclosure containing a finite concentration of atoms, which thermally diffuse through a silicon carbide (SiC) layer over time. No Soret effects, solubility, or trapping effects are included in this case.

This is one of the original problems introduced in Ref. [6] for TMAP4 and adapted in Ref. [7] for TMAP7. Note, however, that the verification cases for TMAP4 and TMAP7, although using the exact same setup, use different quantities to verify their implementation (see Figs. 2(a), 2(b), and 3). In TMAP8, for completeness, we perform verification on all these quantities and show agreement with analytical solutions from both TMAP4 and TMAP7.

##### 3.1.2. Case set up

Fig. 1 shows a schematic of the ver-1a case, along with an illustration of the quantities used for verification. It consists of an enclosure that is pre-charged with a fixed quantity of tritium in gaseous form and a finite SiC slab. At time  $t > 0$ , the tritium is allowed to thermally diffuse through the SiC slab, initially at zero concentration. The surface of the slab in contact with the source is assumed to be in equilibrium with the source enclosure, assuming a temperature-dependent solubility  $S$ . As a boundary condition, the concentration at the outer surface of the SiC slab is kept at zero for all time. The diffusion of the tritium through the SiC slab is calculated by neglecting Soret and trapping effects. Different aspects of the diffusion are compared against analytical solutions, as described below. The values used to characterize the necessary material properties and the case geometry are provided in Table 1.

##### 3.1.3. Verification of the release fraction on the outer surface of the SiC slab (TMAP4)

**3.1.3.1. Analytical solution.** In Ref. [6], i.e., TMAP4, the verification test focused on the fractional release from the outside of the slab. The analytical solution for this quantity is given by

$$FR(t) = 1.0 - \sum_{n=1}^{\infty} \frac{2 L \sec(\alpha_n) \exp(-\alpha_n^2 [Dt/L^2])}{L(L+1) + \alpha_n^2}, \quad (1)$$



**Table 1**  
(Ver-1a) Values of material properties and case geometry with  $R$  the ideal gas constant.

Parameter	Description	Value	Units
$V$	Enclosure volume	$5.20 \times 10^{-11}$	$\text{m}^3$
$A$	SiC slab surface area	$2.16 \times 10^{-6}$	$\text{m}^2$
$P_0$	Initial enclosure pressure	$1 \times 10^6$	Pa
$T$	Temperature	2373	K
$D$	Tritium diffusivity in SiC	$1.58 \times 10^{-4} \times \exp(-308000.0/(RT))$	$\text{m}^2/\text{s}$
$S$	Tritium solubility in SiC	$7.244 \times 10^{22}/T$	$1/\text{m}^3/\text{Pa}$
$l$	Slab thickness	$3.30 \times 10^{-5}$	m

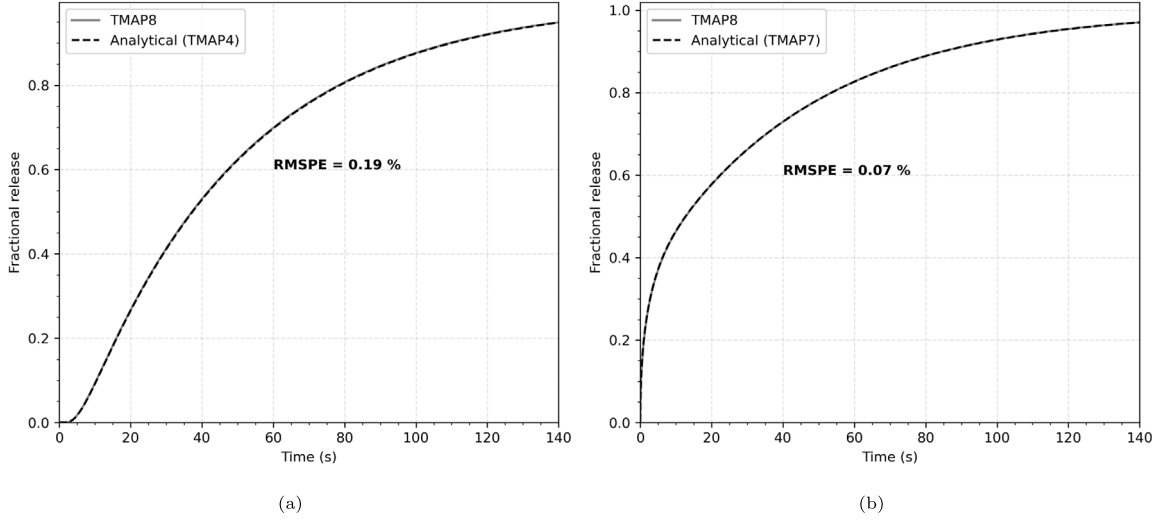


**Fig. 2.** (Ver-1a) Comparison of TMAP8 calculations with analytical solutions for the release fraction on (a) the outer [6] and (b) the inner [7] surface of the SiC slab.

where

$$L = \frac{lA}{V\phi} \quad (2)$$

with

$$\phi = \frac{\text{source concentration}}{\text{layer concentration}} = \frac{1}{Sk_b T}, \quad (3)$$

where the “source concentration” is the concentration in the enclosure ( $P(t)/k_b/T$ ),  $k_b$  is the Boltzmann constant, and “layer concentration” is the concentration in the slab at the interface with the enclosure ( $SP(t)$ ).  $\phi$  is constant in time, and  $\alpha_n$  are the roots of

$$\alpha_n = \frac{L}{\tan \alpha_n}. \quad (4)$$

Note that the expression in Eq. (1) of Ref. [6] writes  $-\alpha_n^2(DT/l^2)$  instead of the correct  $-\alpha_n^2(Dt/l^2)$  in the exponential. If the interested reader needs convincing, analyze the units in the original report for consistency. Despite this typo in the documentation, their results are accurate.

**3.1.3.2. Simulation results.** Fig. 2(a) shows the comparison of the TMAP8 calculation and the analytical solution provided in Ref. [6]. There is agreement between the two plots with a root mean square percentage error (RMSPE) of  $\text{RMSPE} = 0.19\%$  for  $t \geq 1$  s. The RMSPE in this paper is defined as

$$\text{RMSPE} = \frac{\sqrt{\sum (x_{TMAP} - x_{ref})^2/n}}{\sum x_{ref}/n}, \quad (5)$$

where  $x_{TMAP}$  represents the results calculated with TMAP,  $x_{ref}$  represents the reference results obtained from analytical solutions or experiments, and  $n$  is the number of data points. A low RMSPE value signifies a high degree of accuracy.

#### 3.1.4. Verification of the release fraction on the inner surface of the SiC slab (TMAP7)

**3.1.4.1. Analytical solution.** In Ref. [7], i.e., TMAP7, the verification test focuses on the fractional release as determined by the amount of gas release from the enclosure. It is therefore defined as

$$FR(t) = 1.0 - \frac{P(t)}{P_0}, \quad (6)$$

where  $P(t)$  is the pressure at the surface of the enclosure over time. To derive  $FR(t)$ , Ref. [7] first references the analytical solution for an analogous heat transfer problem [53], which provides the solute concentration profile in the membrane as

$$C(x, t) = 2SP_0L' \sum_{n=1}^{\infty} \frac{\exp(-\alpha_n^2 Dt) \sin(\alpha_n x)}{[l(\alpha_n^2 + L'^2) + L'] \sin(\alpha_n l)}, \quad (7)$$

where  $x = l$  is the position of the surface in contact with the enclosure, and  $x = 0$  is the position of the outer surface (as defined in Ref. [7]),

$$L' = \frac{STAk_b}{V}, \quad (8)$$

and  $\alpha_n$  are the roots of

$$\alpha_n = \frac{L}{\tan(\alpha_n l)}. \quad (9)$$

By linking the concentration on the surface of the slab in contact with the enclosure ( $x = l$  as used in Ref. [7]) with the pressure of the enclosure, Henry's law provides

$$P(t) = \frac{C(l, t)}{S} = 2P_0L' \sum_{n=1}^{\infty} \frac{\exp(-\alpha_n^2 Dt)}{l(\alpha_n^2 + L'^2) + L'}, \quad (10)$$

which leads to

$$FR(t) = 1.0 - \frac{P(t)}{P_0} = 1 - 2L' \sum_{n=1}^{\infty} \frac{\exp(-\alpha_n^2 Dt)}{l(\alpha_n^2 + L'^2) + L'}. \quad (11)$$

There are a few issues in the documentation of this verification case in Ref. [7]:

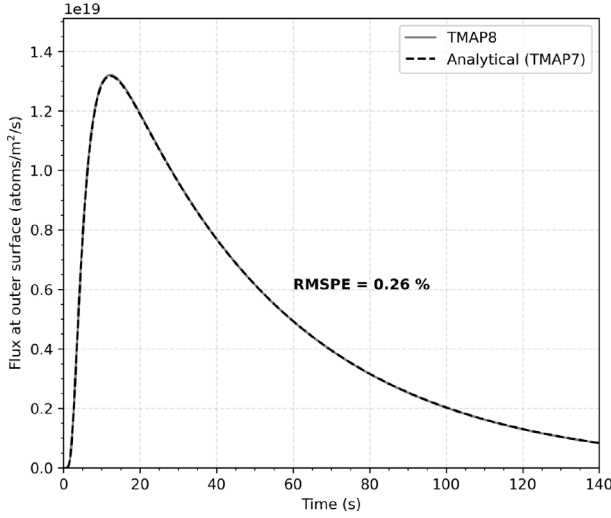


Fig. 3. (Ver-1a) Comparison of TMAP8 calculation with the analytical solution for the tritium flux at the outer surface of the SiC slab [7].

- The units and expression of the solubility provided in Ref. [7] have typos. The correct values and units are provided above in Table 1. The value provided in Ref. [7] is  $S = 3.053 \times 10^{29}$  kg m<sup>2</sup>/s<sup>2</sup> instead of  $S = 7.244 \times 10^{22}/T = 3.053 \times 10^{19}$  1/m<sup>3</sup>/Pa when  $T = 2373$  K. The correct value of  $S$  is used in the input file decks in [6,7].
- The release fraction in Ref. [7] is described as  $P(t)/P_0$  in their Eq. (5) but is actually plotted as  $1 - (P(t)/P_0)$  in Figure 1 of that report.
- A potential source of confusion is that in Ref. [7],  $x = 0$  represents the surface not exposed to the enclosure (where  $c = 0$ ), and  $x = l$  represents the surface exposed to the enclosure. In the TMAP8 documentation, we have kept this convention to correspond to the TMAP7 case, but note that the TMAP8 input file fixes  $x = 0$  at the enclosure surface and  $x = l$  for the outer surface.

**3.1.4.2. Simulation results.** Fig. 2(b) shows the comparison of the TMAP8 calculation and the analytical solution for release fraction provided in Ref. [7]. There is agreement between the two plots with RMSPE = 0.07% for  $t \geq 1$  s.

### 3.1.5. Verification of the tritium flux at the outer surface of the SiC slab (TMAP7)

**3.1.5.1. Analytical solution.** In Ref. [7], i.e., TMAP7, the verification test also tests the model's accuracy in determining the tritium flux across the outer surface of the SiC slab. Using the expression of the concentration provided above, the flux on the outer surface of the SiC slab can be derived as

$$J(t) = D \frac{\partial C(x, t)}{\partial x} \Big|_{x=0} = 2SP_0L'D \sum_{n=1}^{\infty} \frac{\exp(-\alpha_n^2 Dt) \alpha_n}{[l(\alpha_n^2 + L'^2) + L'] \sin(\alpha_n l)}, \quad (12)$$

which can be compared to TMAP8 predictions. Again, be aware of the typos in Ref. [7] and the different coordinates used in TMAP8 and TMAP7 discussed above.

**3.1.5.2. Simulation results.** Fig. 3 shows the comparison of the TMAP8 calculation and the analytical solution for flux at the outer surface of the SiC slab in Ref. [7]. There is agreement between the two plots with RMSPE = 0.26% for  $t \geq 1$  s.

## 3.2. Ver-1b: Diffusion problem with constant source boundary condition

This verification problem is taken from Ref. [6]. Diffusion of tritium through a semi-infinite SiC layer is modeled with a constant source

located on one boundary. No solubility or trapping is included. The concentration as a function of time and position is given by

$$C = C_0 \operatorname{erfc} \left( \frac{x}{2\sqrt{Dt}} \right), \quad (13)$$

where  $C_0$  the constant source concentration,  $\operatorname{erfc}$  is the complementary error function,  $x$  is the distance from the boundary,  $D$  is the diffusion coefficient, and  $t$  is the time.

Comparison of the TMAP8 results and the analytical solution is shown in Fig. 4(a) as a function of time at  $x = 0.2$  mm. For simplicity, both the diffusion coefficient and the initial concentration were set to unity. The TMAP8 code predictions match the analytical solution very well. As an additional check, the concentration as a function of position at a given time  $t = 25$  s calculated by TMAP8 was compared with the analytical solution as shown in Fig. 4(b). The predicted concentration profile from TMAP8 is in good agreement with the analytical solution.

Finally, the diffusive flux ( $J$ ) is compared with the analytic solution where the flux is proportional to the derivative of the concentration with respect to  $x$  and is given by

$$J = C_0 \sqrt{\frac{D}{t\pi}} \exp \left( \frac{x}{2\sqrt{Dt}} \right). \quad (14)$$

The flux as given by Eq. (14) is compared with values calculated by TMAP8. The diffusivity,  $D$ , and the initial concentration,  $C_0$ , were both taken as unity, and the distance,  $x$ , was taken as 0.5 in this comparison. TMAP8 initially underpredicts, but the results match well subsequently. Comparison results are shown in Fig. 5 with RMSPE = 6.03%. The error is calculated for  $t \geq 10$  s due to infinite value at small  $t$ .

## 3.3. Ver-1c: Diffusion problem with partially preloaded slab

This verification problem is taken from Refs. [6,7]. Diffusion of tritium through a semi-infinite SiC layer is modeled with an initial loading of 1 atom/m<sup>3</sup> in the first 10 m of a 100 m slab. TMAP4 uses a slab length of 2275 m (the slab length is not specified in the TMAP7 document [7]); however, using a smaller slab length was found not to change the results. Additionally, the smaller domain size allows getting a finer simulation mesh for the same computational cost, which improves the agreement between the TMAP8 and analytical calculations.

Diffusivity is set to 1 m<sup>2</sup>/s and no trapping is included. TMAP4 and TMAP7 also use different boundary conditions for the left side of the slab (at  $x = 0$  m). In TMAP4, an insulating boundary condition is used, and the analytical solution is given by [53]

$$C(x, t) = \frac{C_0}{2} \left[ \operatorname{erf} \left( \frac{h-x}{2\sqrt{Dt}} \right) + \operatorname{erf} \left( \frac{h+x}{2\sqrt{Dt}} \right) \right], \quad (15)$$

but TMAP7 uses a zero-concentration boundary condition, with the analytical solution given by [53]

$$C(x, t) = \frac{C_0}{2} \left[ 2\operatorname{erf} \left( \frac{x}{2\sqrt{Dt}} \right) - \operatorname{erf} \left( \frac{x-h}{2\sqrt{Dt}} \right) - \operatorname{erf} \left( \frac{x+h}{2\sqrt{Dt}} \right) \right], \quad (16)$$

where  $h = 10$  m is the thickness of the preloaded portion of the layer,  $C_0$  is the initial concentration in the preloaded section of the slab,  $\operatorname{erf}$  is the error function,  $x$  is the position along the slab, and  $D$  is the diffusivity. Note that Eq. (15) differs from the solution provided in Ref. [6] because of a typographical error, instead we use the analytical solution found in Ref. [53], which produces the theoretical results found in Tables 15-17 of Ref. [6].

TMAP4 and TMAP7 verification cases are evaluated at different points. TMAP4 verifies the mobile species concentration at three points: (a) a point at the free surface ( $x = 0$  m), (b) a point at the end of the preloaded region ( $x = 10$  m), and (c) a point in the initially unloaded region ( $x = 12$  m). The comparison of the values calculated with TMAP8 and analytically for the TMAP4 cases is shown in Fig. 6(a). TMAP7

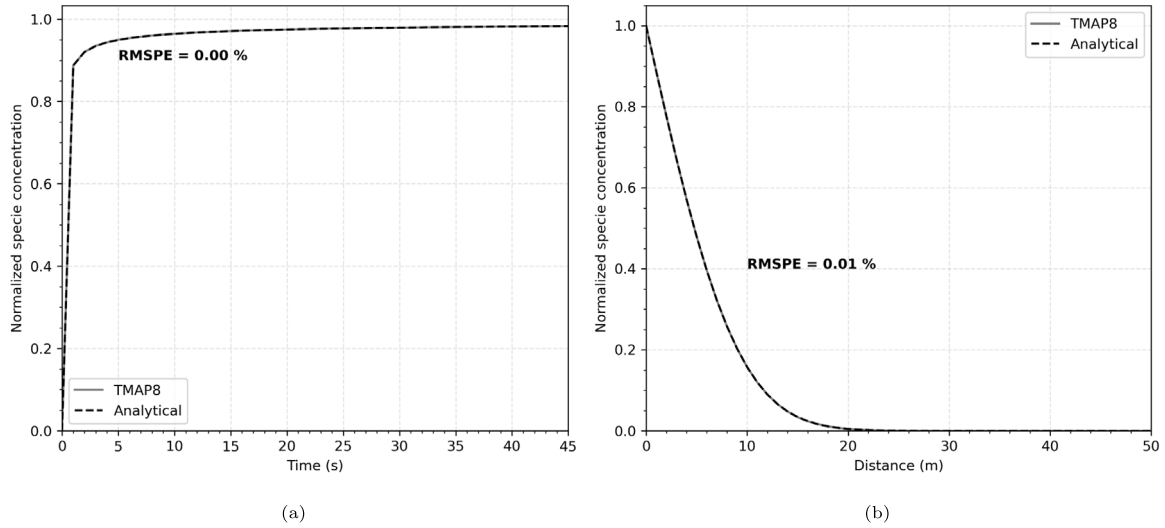


Fig. 4. (Ver-1b) Comparison of concentration as function of (a) time at  $x = 0.2$  m and (b) distance at  $t = 25$  s calculated through TMAP8 and analytically.

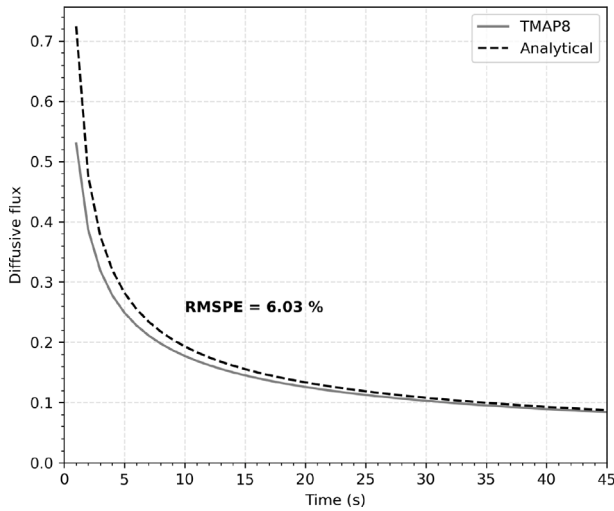


Fig. 5. (Ver-1b) Comparison of flux as function of time at  $x = 0.5$  m calculated through TMAP8 and analytically.

verifies the mobile species concentration at the same points (b) and (c) as in the TMAP4 case, but as the concentration at the free surface is specified, it performs the third comparison (d) a point close to the free surface ( $x = 0.25$  m). The comparison of the values calculated with TMAP8 and analytically for the TMAP7 cases is shown in Fig. 6(b). In all cases, the TMAP8 calculations are found to be in good agreement with the analytical solution.

### 3.4. Ver-1d: Permeation problem with and without trapping

This verification problem exercises TMAP8's ability to accurately model permeation through a membrane with a constant source. It is taken from Refs. [6,7]. This verification case tests different scenarios for permeation, namely (1) without trapping, (2) with trapping in the diffusion-limited regime, (3) with trapping in the trapping-limited regime, and (4) with multiple trapping site populations. These sub-cases challenge TMAP8 in different situations relevant to real-life systems, and TMAP8's predictions are compared to analytical solutions to evaluate its accuracy.

#### 3.4.1. Ver-1d: Permeation problem without trapping

This verification problem is taken from Ref. [7] and captures simple diffusion across a membrane. We solve the following equation

$$\frac{dC_M}{dt} = \nabla D \nabla C_M, \quad (17)$$

where  $C_M$  is the mobile concentration,  $t$  is the time, and  $D$  is the diffusivity of the mobile species defined as

$$D(T) = D_0 \exp\left(-\frac{E_a}{k_B T}\right), \quad (18)$$

where  $T$  is the temperature in Kelvin and  $k_B = 1.380649 \times 10^{-23}$  J/K is the Boltzmann constant.

Ref. [7] provides the analytical equations for the permeation transient as

$$J_p = \frac{C_0 D}{l} \left\{ 1 + 2 \sum_{m=1}^{\infty} \left[ (-1)^m \exp\left(-m^2 \frac{t}{2 \tau_{be}}\right) \right] \right\}, \quad (19)$$

where  $C_0$  is the steady dissolved gas concentration at the upstream ( $x = 0$ ) side,  $l$  is the thickness of the slab,  $D$  is the diffusivity of the gas through the material, and  $\tau_{be}$  is the breakthrough time. The breakthrough time is defined as the intersection of the steepest tangent to the diffusion transient with the time axis and is expressed as

$$\tau_{be} = \frac{l^2}{2 \pi^2 D_{eff}}, \quad (20)$$

where  $D_{eff}$ , the effective diffusivity, is equal to  $D$  due to the absence of traps in the membrane. The model parameter values are listed in Table 2.

The analytical solution for the permeation transient is compared with TMAP8 results in Fig. 7. The graphs for the analytical flux and the calculated flux are in good agreement, with RMSPE = 0.14% for  $t \geq 0.01$  s. The breakthrough time calculated from the analytical solution provided by Eq. (20) is 0.05 s, and the breakthrough time from TMAP8 is 0.05 s, which matches.

#### 3.4.2. Ver-1d: Permeation problem with trapping

This verification case expands the case described in Section 3.4.1 by introducing one trapping site population. It was first introduced in Ref. [6] and also used in Ref. [7]. Since the model now includes trapping, Eq. (17) is extended to a system of coupled equations accounting for trapping, as

$$\frac{dC_M}{dt} = \nabla D \nabla C_M - \text{trap\_per\_free} \cdot \frac{dC_T}{dt}, \quad (21)$$

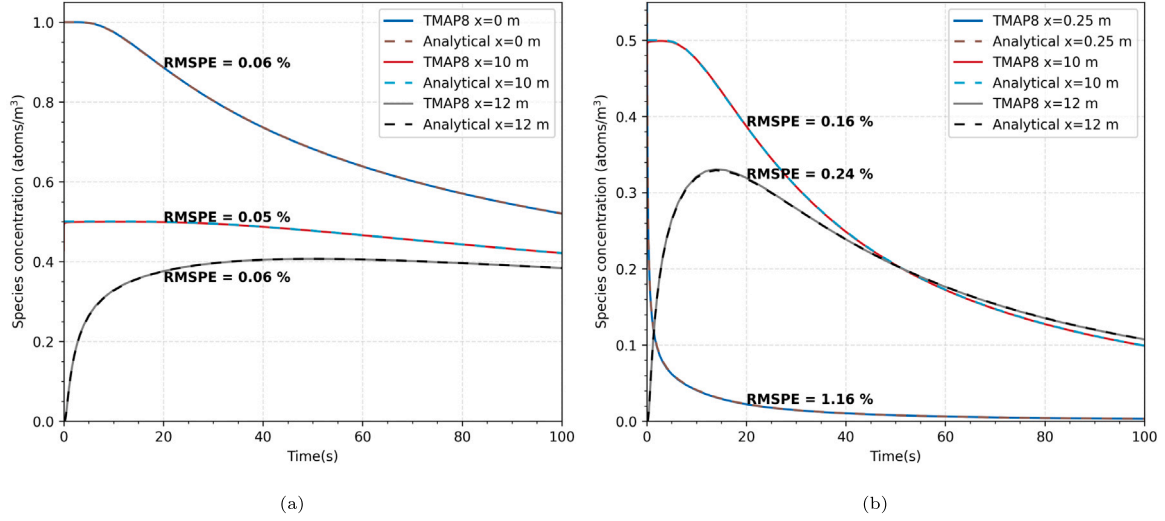


Fig. 6. (Ver-1c) Comparison of concentration as a function of time at (a)  $x = 0$  m, 10 m, and 12 m (TMAP4 cases) and at (b)  $x = 0.25$  m, 10 m, and 12 m (TMAP7 cases) calculated with TMAP8 and analytically.

Table 2

Parameter values ver-1d sub-cases, including (1) without trapping, (2) with trapping in the diffusion-limited regime, (3) with trapping in the trapping-limited regime, and (4) with multiple trapping site populations.

Parameter	No Trap.	Diffusion-Limited	Trap.-Limited	Multiple Trap.	Units
$l$	1	Identical	Identical	Identical	m
$D_0$	1	Identical	Identical	Identical	m²/s
$E_d$	0	Identical	Identical	Identical	J
$N$	$3.1622 \times 10^{22}$	Identical	Identical	Identical	at/m²
$C_0$	$3.1622 \times 10^{18}$	Identical	Identical	Identical	at/m²
$T$	—	1000	Identical	Identical	K
$\lambda$	—	$\sqrt{10^{-15}}$	Identical	Identical	m
$\nu$	—	$10^{13}$	Identical	Identical	s⁻¹
$C_{T0}$	—	0.1	0.1	0.1, 0.15, and 0.20	(—)
$\epsilon/k_B$	—	100	10 000	100, 500, and 800	K

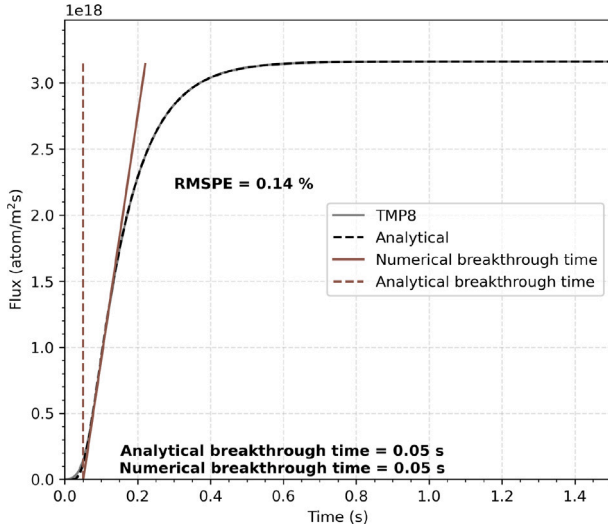


Fig. 7. (Ver-1d) Comparison of TMAP8 calculation with the analytical solution for the permeation transient without traps from Ref. [7].

$$\frac{dC_T}{dt} = \alpha_i \frac{C_T^{empty} C_M}{(N \cdot \text{trap\_per\_free})} - \alpha_r C_T, \quad (22)$$

and

$$C_T^{empty} = C_{T0} \cdot N - \text{trap\_per\_free} \cdot C_T, \quad (23)$$

where  $C_T$  is the concentration of the trapped species,  $\alpha_i$  and  $\alpha_r$  are the trapping and release rate coefficients,  $\text{trap\_per\_free}$  is a factor converting the magnitude of  $C_T$  to be closer to  $C_M$  for better numerical convergence,  $C_{T0}$  is the fraction of host sites that can contribute to trapping,  $C_T^{empty}$  is the concentration of empty trapping sites, and  $N$  is the host density.

The breakthrough time may have one of two limiting values depending on whether the trapping is in the effective diffusivity or strong-trapping regime. A trapping parameter is defined by

$$\zeta = \frac{\lambda^2 \nu}{C_{T0} D_0} \exp\left(\frac{E_d - \epsilon}{kT}\right) + \frac{C_f}{C_{T0}}, \quad (24)$$

where  $\lambda$  is the lattice parameter,  $\nu$  is the Debye frequency,  $\epsilon$  is the trapping energy, and  $C_f$  is the gas atom fraction.

The discriminant for which regime is dominant is the ratio of  $\zeta$  to  $C_f/C_{T0}$ . If  $\zeta \gg C_f/C_{T0}$ , then the effective diffusivity regime applies, and the permeation transient is identical to the standard diffusion transient presented in Section 3.4.1 but with the diffusivity replaced by the effective diffusivity

$$D_{eff} = \frac{D}{1 + \frac{1}{\zeta}} \quad (25)$$

to account for the fact that trapping leads to slower transport. In this limit, the breakthrough time will be defined as in Eq. (20). The permeation transient flux is then given by Eq. (19).

In the deep-trapping limit,  $\zeta \approx C_f/C_{T0}$ , and no permeation occurs until essentially all the traps have been filled. Then the system quickly reaches steady-state. The breakthrough time is given by

$$\tau_{bd} = \frac{l^2 C_{T0}}{2 C_0 D}, \quad (26)$$



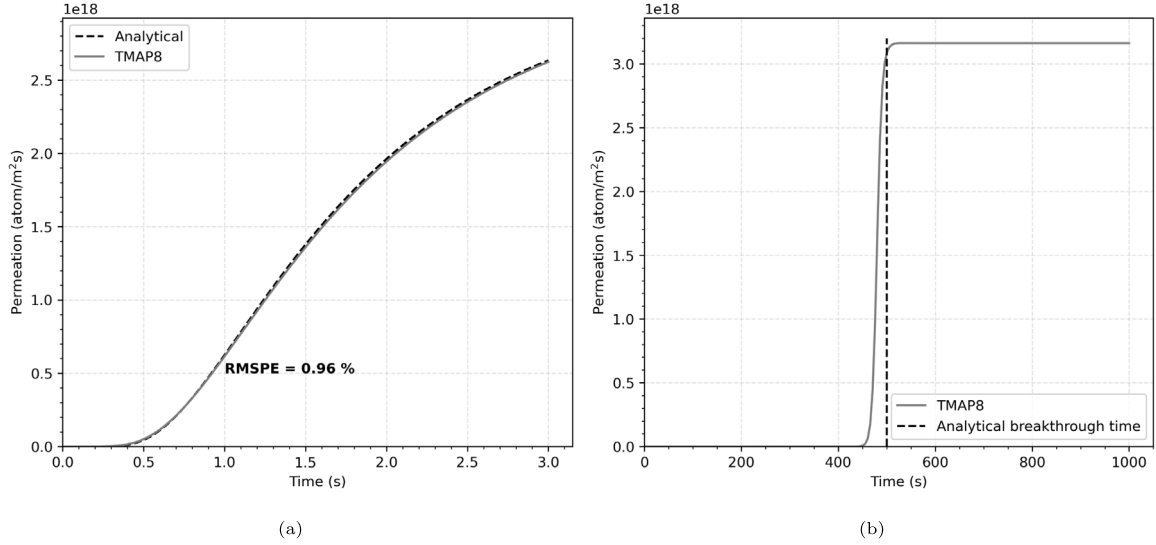


Fig. 8. (Ver-1d) Comparison of TMAP8 calculation with the analytical solution for the permeation transient in a slab with (a) diffusion-limited trapping and (b) strong trapping.

where  $C_0$  is the steady dissolved gas concentration at the upstream ( $x = 0$ ) side.

Using TMAP8, we examine these two different regimes, one where diffusion is the rate-limiting step and one where trapping is the rate-limiting step. The model parameter values used in both cases are provided in Table 2. For the diffusion limited regime, we selected  $\epsilon/k = 100$  K to give  $\zeta = 91.47C_f/C_{T0}$ . The comparison results are presented in Fig. 8(a) with RMSPE = 0.96% for  $t \geq 0.4$  s. For the deep-trapping limit, we selected  $\epsilon/k = 10000$  K to give  $\zeta = 1.00454C_f/C_{T0}$ . The comparison results are presented in Fig. 8(b).

While simulating this case in TMAP8, we realized that this simulation can generate oscillations in the solution due to the feedback loop between the diffusion and trap evolution equations (see Eqs. (21) and (22)). In order for the oscillations to not take over the simulation, it seems that the ratio of the inverse of the Fourier number must be kept sufficiently high, e.g.,  $h^2/(Ddt) \gg 1$ . The oscillations in the permeation graph go away with increasing fineness in the mesh and in the time step  $dt$ . To keep the oscillations damped, this verification case is run with 1000 nodes in the mesh and an adaptive time stepper with an initial time step of  $10^{-6}$  s. Additionally, the boundary condition on the diffusion variable  $C_M$  is increased gradually from the initial condition value of the variable (zero) to one over using the function

$$C_M(x=0) = \tanh(3t). \quad (27)$$

This takes the boundary condition to 99.5% of its actual value in 3 s, which is a small fraction of the breakthrough time of 500 s. It therefore reduces numerical oscillations without affecting the expected solution.

### 3.4.3. Ver-1d: Permeation problem with multiple trapping

**3.4.3.1. Verification by comparison against analytical solutions.** This verification problem is taken from Ref. [7] and builds on the capabilities verified in Sections 3.4.1 and 3.4.2. It extends the previous cases to three different trapping types with different properties. This verification case was first introduced in Ref. [7] to highlight TMAP7's capability to model up to three different trapping populations, when TMAP4 was limited to one [6]. However, TMAP8 can accommodate an arbitrary number of trapping populations.

To capture the additional trapping populations, Eqs. (21) and (22) are updated into

$$\frac{dC_M}{dt} = \nabla D \nabla C_M - \text{trap\_per\_free} \cdot \sum_{i=1}^3 \frac{dC_{T_i}}{dt}, \quad (28)$$

and, for  $i = 1, i = 2$ , and  $i = 3$ ,

$$\frac{dC_{T_i}}{dt} = \alpha_i^i \frac{C_{T_i}^{\text{empty}} C_M}{(N \cdot \text{trap\_per\_free})} - \alpha_r^i C_{T_i}, \quad (29)$$

and

$$C_{T_i}^{\text{empty}} = (C_{T0} \cdot N - \text{trap\_per\_free} \cdot C_{T_i}), \quad (30)$$

where  $C_{T_i}$  is the trapped species in trap  $i$ ,  $\alpha_i^i$  and  $\alpha_r^i$  are the trapping and release rate coefficients for trap  $i$ ,  $\text{trap\_per\_free}$  is a factor scaling  $C_{T_i}$  to be closer to  $C_M$  for better numerical convergence,  $C_{T0}$  is the fraction of host sites  $i$  that can contribute to trapping, and  $C_{T_i}^{\text{empty}}$  is the concentration of empty trapping sites. The trapping parameter is defined by

$$\zeta = \frac{\lambda^2 v}{C_{T0} D_0} \exp\left(\frac{E_d - \epsilon}{kT}\right) + \frac{C_f}{C_{T0}}. \quad (31)$$

The analytical expression for the permeation transient flux is again defined by Eq. (19). The effective diffusivity  $D_{eff}$ , which influences the breakthrough time  $\tau_{b_e}$  defined in Eq. (20), is now defined as

$$D_{eff} = \frac{D}{1 + \sum_{i=1}^3 1/\zeta_i}, \quad (32)$$

where  $\zeta_i$  is the trapping parameter of trap  $i$ . The parameter values are provided in Table 2. The trapping parameters,  $\zeta_i$ , calculated from Eq. (24) for the three traps are  $91.47930 C_f/C_{T0}$ ,  $61.65009 C_f/C_{T0}$ , and  $45.93069 C_f/C_{T0}$ . Note that the  $\zeta_i$  values of the three traps from Ref. [7] have a typographical error. They are three orders of magnitude lower than the correct values. However, it does not impact the final analytical solution.

The analytical solution for the permeation transient is compared with TMAP8 results in Fig. 9. The graphs for the theoretical flux and the calculated flux are in good agreement, with RMSPE = 0.41% for  $t \geq 3$  s. The breakthrough time calculated from Eq. (20) in analytical solution is 4.04 s, and the breakthrough time from TMAP8 is 4.12 s, which is close.

**3.4.3.2. Further verification using the method of manufactured solutions (MMS).** Although the flux and breakthrough time can be verified using analytical solutions as presented above, the MMS approach is a powerful method to verify complex system of PDEs such as the one studied in this case. Here, we apply the MMS approach available as a Python-based utility in the MOOSE framework [45,54] to verify TMAP8's predictions for ver-1d through spatial convergence. Below,

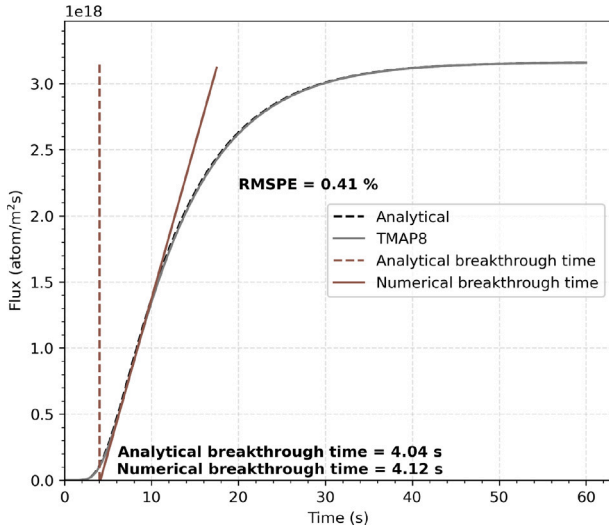


Fig. 9. (Ver-1d) Comparison of TMAP8 calculation with the analytical solution for the permeation transient with multiple trapping from [7].

we detail how we apply the MMS approach to this case coupling diffusion and multiple trapping and discuss the results, which verify these capabilities.

A detailed and step by step description of the MMS approach is available on the online MOOSE documentation; we present here a short description. To perform a spatial convergence study with the MMS, we select a smoothly-varying sinusoidal spatial solution for the mobile and trapped species. In order to prevent temporal error from polluting the spatial error, we pick a temporal dependence that can be exactly represented by the time integrator we choose. In this MMS case, we use implicit or backwards Euler which is first-order accurate; consequently we choose a linear dependence on time. For our 1D case, this leads us to select the following MMS solution for the mobile species:

$$u(x, t) = \cos(x)t, \quad (33)$$

with  $x$  the position along the 1D domain, and  $t$  the time. The trapping species concentrations are represented similarly with, for  $i = 1$ ,  $i = 2$ , and  $i = 3$ :

$$u_i(x, t) = \frac{Nu_{i,0}}{2}(t \cos(x) + 1), \quad (34)$$

with  $u_{i,0}$  the equivalent of  $C_{T0}$  in Eq. (30).

With the manufactured solutions selected, we generate forcing functions  $f$  and  $f_i$  by substituting the exact solutions into the strong-form PDEs, Eqs. (A.1) and (A.2). Assuming  $\text{trap\_per\_free} = 1$ , this leads to

$$\frac{\partial u}{\partial t} - \nabla \cdot (D \nabla u) + \sum_{i=1}^3 \frac{\partial u_i}{\partial t} - f = 0, \quad (35)$$

and, for  $i = 1$ ,  $i = 2$ , and  $i = 3$ ,

$$\frac{\partial u_i}{\partial t} - \alpha_i^i \frac{u_i^{\text{empty}}}{N} + \alpha_r^i u_i - f_i = 0. \quad (36)$$

$f$  and  $f_i$  are therefore defined as

$$f = \cos(x) + Dt \cos(x) + \sum_{i=1}^3 \frac{Nu_{i,0}}{2} \cos(x), \quad (37)$$

and, for  $i = 1$ ,  $i = 2$ , and  $i = 3$ ,

$$f_i = \frac{u_{i,0}}{2} (N \cos(x) + \alpha_r^i N(t \cos(x) + 1) - \alpha_i^i t \cos(x)(-t \cos(x) + 1)). \quad (38)$$

Eqs. (35) and (36) now form a system of equation that can be solved and compared against the exact solutions defined in Eqs. (33) and (34). Dirichlet boundary conditions for the mobile species are imposed using the selected exact/MMS solution. For the spatial discretization, we

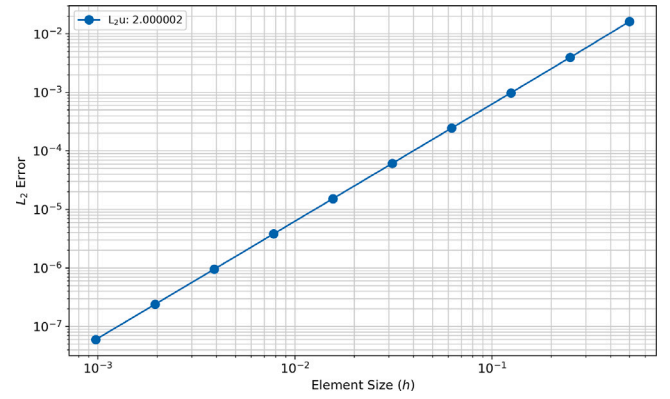


Fig. 10. (Ver-1dc) Spatial convergence from the MMS for a diffusion-trapping-release problem modeled after the physics of ver-1d using first order Lagrange basis functions. The expected quadratic convergence rate of the  $L_2$  error is observed.

select first order Lagrange basis functions for the mobile concentration and for projecting the trapped species concentrations from nodes into element interiors for coupling in the trapped specie time derivative term in the mobile specie governing equation.

The results of the spatial convergence study using the MMS is shown in Fig. 10, with 10 levels of refinement. The expected quadratic convergence rate of the  $L_2$  error is observed since the slope is equal to  $2 + 2 \times 10^{-6}$ , which is close to 2. This therefore verifies the proper implementation of the diffusion and multi-trapping capabilities. The results are consistent with the MMS study presented in Ref. [55].

### 3.5. Ver-1e: Diffusion in composite material layers

#### 3.5.1. Case description

This verification problem is taken from Refs. [6,7]. In this problem, a composite structure of PyC and SiC is modeled with a constant concentration boundary condition of the free surface of PyC and zero concentration boundary condition on the free surface of the SiC.

#### 3.5.2. Analytical solution at steady state

The steady-state solution for the PyC is given in [6,7] as

$$C = C_0 \left[ 1 + \frac{x}{l} \left( \frac{aD_{PyC}}{aD_{PyC} + lD_{SiC}} - 1 \right) \right], \quad (39)$$

while the concentration profile for the SiC layer is given as

$$C = C_0 \left( \frac{a+l-x}{l} \right) \left( \frac{aD_{PyC}}{aD_{PyC} + lD_{SiC}} \right), \quad (40)$$

where  $C$  is the concentration,  $x$  is the distance from free surface of PyC,  $a$  is the thickness of the PyC layer (33  $\mu\text{m}$ ),  $l$  is the thickness of the SiC layer (63  $\mu\text{m}$  in the TMAP4 verification case and 66  $\mu\text{m}$  in the TMAP7 verification case),  $C_0$  is the concentration at the PyC free surface (50.7079 mol/m<sup>3</sup>),  $D_{PyC}$  is the diffusivity in PyC ( $1.274 \times 10^{-7}$  m<sup>2</sup>/s), and  $D_{SiC}$  is the diffusivity in SiC ( $2.622 \times 10^{-11}$  m<sup>2</sup>/s).

#### 3.5.3. Analytical solution during transient

The analytical transient solution for the concentration in the PyC and SiC blocks as function of position and time is taken from Table 3, row 1 in Ref. [56]. It is given as

$$C = C_0 \left\{ \frac{(a-x)D_{SiC} + lD_{PyC}}{lD_{PyC} + aD_{SiC}} - 2 \sum_{n=1}^{\infty} B_n \sin\left(\lambda_n \frac{x}{a}\right) \exp\left(-D_{PyC} \frac{\lambda_n^2}{a^2} t\right) \right\}, \quad (41)$$

$$B_m = \frac{D_{PyC} l \sin^2(k\lambda_n l/a) (\cos(\lambda_n) - 1) + D_{SiC} \sin(k\lambda_n l/a) (kl \sin(\lambda_n) \cos(k\lambda_n l/a) - a \sin(k\lambda_n l/a))}{\lambda_n (a D_{SiC} + l D_{PyC}) (\sin^2(k\lambda_n l/a) + l/a \sin^2(\lambda_n))}, \quad (44)$$

Box I.

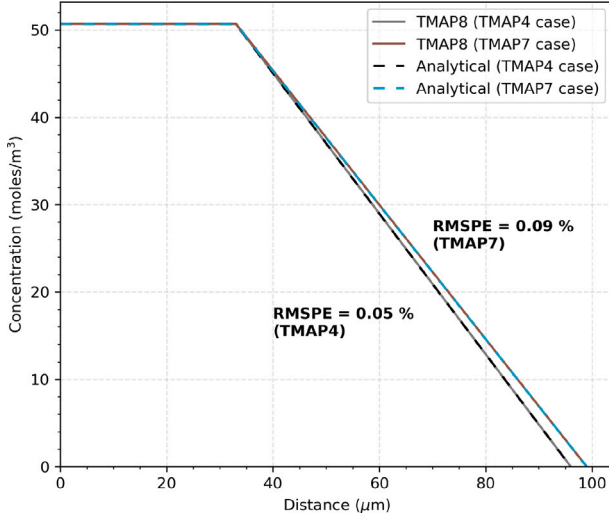


Fig. 11. (Ver-1e) Comparison of TMAP8 calculation with the analytical solution for concentration at steady state. The RMSPE between the TMAP8 prediction and analytical solution for the TMAP4 and TMAP7 verification cases is low.

and

$$C = C_0 \left\{ \frac{(l + a - x) D_{PyC}}{l D_{PyC} + a D_{SiC}} - 2 \sum_{n=1}^{\infty} B_m \frac{\sin(\lambda_n)}{\sin(k\lambda_n l/a)} \sin\left(k\lambda_n \frac{l + a - x}{a}\right) \times \exp\left(-D_{PyC} \frac{\lambda_n^2}{a^2} t\right) \right\}, \quad (42)$$

where (see the Eq. (44) in Box I).

$$k = \sqrt{\frac{D_{PyC}}{D_{SiC}}}, \quad (43)$$

and  $\lambda_n$  are the roots of

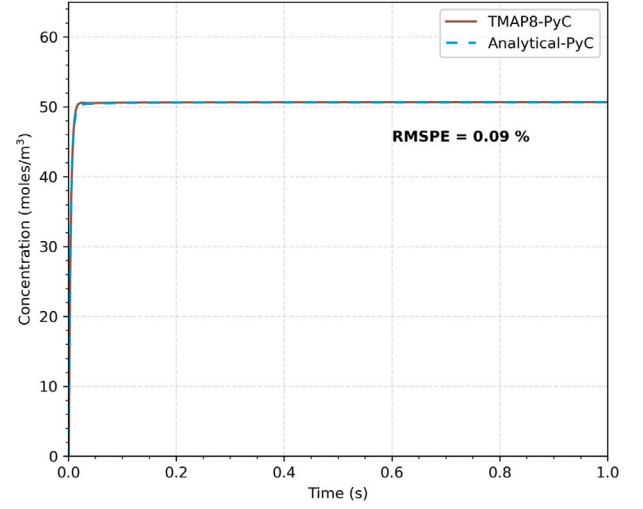
$$\frac{\sin(\lambda_n) \cos(k\lambda_n l/a)}{k} + \cos(\lambda_n) \sin(k\lambda_n l/a) = 0. \quad (45)$$

Note that the expressions of the analytical solution for the transient case in TMAP4 [6] and TMAP7 [7] are inconsistent with the results, which suggest typographical errors. Moreover, no reference is provided. For these reasons, we use a different analytical transient solution and roots of  $\lambda_n$  for the concentration in PyC and SiC layer from Refs. [56], as listed in Eqs. (41) to (45).

### 3.5.4. Simulation results

Fig. 11 shows the comparison of the TMAP8 calculation and the analytical solution for concentration after steady state is reached. The plots show the TMAP8 and analytical solution comparisons for both the TMAP4 case ( $l = 63 \mu\text{m}$ ) and the TMAP7 case ( $l = 66 \mu\text{m}$ ).

To verify the transient solutions, we select two different points: One in the PyC layer at  $x = 32 \mu\text{m}$ , and one in the SiC layer. The concentration at these two points is calculated using TMAP8 and with the analytical equations (Eqs. (41) and (42)). Fig. 12(a) shows the comparison of the TMAP8 calculation against the analytical solution for this transient case in the PyC layer from 0 s to 1 s. Note that we only use the parameters from TMAP7 because the trivial difference between



(a)

Fig. 12. (Ver-1e) Comparison of TMAP8 calculation against the analytical solution for the transient diffusion at  $x = 32 \mu\text{m}$  in PyC layer for  $0 \text{ s} < t < 1 \text{ s}$ . The RMSPE between the TMAP8 prediction and analytical solution for TMAP7 verification cases is low.

TMAP4 and TMAP7 in the PyC layer. Fig. 13(a) shows the comparison of the TMAP calculation against the analytical solution in the SiC layer. In the TMAP4 case,  $x = 41 \mu\text{m}$ , and in the TMAP7 case,  $x = 48.75 \mu\text{m}$ . There is good agreement between TMAP8 and the analytical solution for both steady-state and transient cases. In both cases, the RMSPE is under 0.2%. The error is calculated between the TMAP8 and analytical solution values after  $t = 0.2 \text{ s}$ . This is in order to ignore the unphysical predictions of the analytical solution at very small time, as shown in Fig. 13(b), which is a close-up view of Fig. 13(a) at the start of the simulation. The departure from physical results at low  $t$  is due to the limited number of  $\lambda_n$  values being used from Eq. (45). We use  $\lambda_n$  values ranging from 0 to 100. Using  $\lambda_n$  values in a larger range would only have limited improvement in the accuracy but increase the running time for the computation of the analytical solutions.

## 3.6. Ver-1f: Heat conduction with heat generation and thermal transient

### 3.6.1. Case description

This heat transfer verification problem is taken from Refs. [6,7]. This case models a heat conduction problem through a slab with two different variants. The first variant, ver-1fa, includes a heat source. The second variant, ver-1fb, has no heat source, but its temperature boundary conditions are such that the sample is under transient conditions under a temperature gradient. In both cases, the heat conduction in the 1D model is described as

$$\rho C_p \frac{dT}{dt} = \nabla k \nabla T + Q, \quad (46)$$

where  $T$  is the temperature,  $\rho$  is the density,  $C_p$  is the specific heat,  $k$  is the thermal conductivity, and  $Q$  is the internal volumetric heat generation rate.

The model parameter values for both cases are provided in Table 3. In case ver-1fa, one end of the slab is kept at a constant temperature of

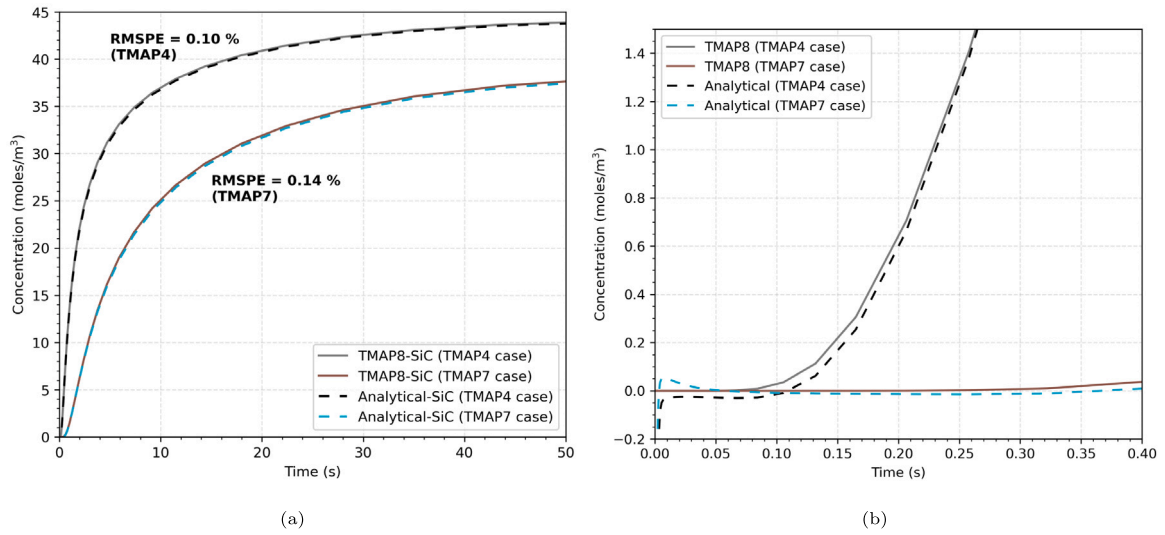


**Fig. 13.** (Ver-1e) Comparison of TMAP8 calculations with the analytical solution for the transient diffusion in SiC layer (a) for  $0 \leq t < 50$  s, and (b) for  $t < 0.4$  s. The positions of interest are  $x = 41 \mu\text{m}$  for the TMAP4 case and  $x = 48.75 \mu\text{m}$  for the TMAP7 case. The RMSPE between the TMAP8 predictions and the analytical solutions are low. In (b), the analytical solution shows unphysical predictions close to  $t = 0$  s, whereas TMAP8's predictions are reasonable.

**Table 3**

Model parameter values for ver-1fa and ver-1fb [6,7].

Parameter	ver-1fa	ver-1fb	Units
$L$	1.6	4.0	m
$k$	10	10	W/m/K
$\rho$	1	1	kg/m <sup>3</sup>
$C_p$	1	10	J/kg/K
$Q$	$1 \times 10^4$	–	W/m <sup>3</sup>

300 K while the other end acts as an adiabatic surface. In case ver-1fb, the ends of a slab are kept fixed at different temperatures, namely 400 K and 300 K. The temperature distribution in the slab evolves from an initial state to steady state.

### 3.6.2. Analytical solution

For case ver-1fa (heat conduction with a heat source), Ref. [57] provides the analytical solution for the steady-state temperature as

$$T = T_s + \frac{QL^2}{2k} \left( 1 - \frac{x^2}{L^2} \right), \quad (47)$$

where  $L$  is the thickness of the slab, and  $T_s$  is the imposed surface temperature.

For case ver-1fb (heat conduction during a transient), Ref. [57] provides the analytical solution for the temperature as

$$T(x, t) = T_0 + (T_1 - T_0) \left\{ 1 - \frac{x}{L} - \frac{2}{L} \sum_{m=1}^{\infty} \left( \frac{1}{\lambda_m} \sin(\lambda_m x) \exp(-\alpha \lambda_m^2 t) \right) \right\}, \quad (48)$$

where  $x$  is the distance across the slab,  $t$  is the time,  $\lambda_m$  is a multiple of  $\frac{m\pi}{L}$ , and  $\alpha$  is the thermal diffusivity, which is defined as

$$\alpha = \frac{k}{\rho C_p}. \quad (49)$$

Both TMAP4 [6] and TMAP7 [7] provide analytical solutions for the transient case, but they use different equations. At the initial time and steady state, the solution from TMAP7 matches the real thermal distribution, whereas the solution from TMAP4 does not. Thus, TMAP8 selects the solution from TMAP7 as the analytical solution (see Eq. (48)).

### 3.6.3. Simulation results

A comparison of the temperature distribution in the slab, computed through TMAP8 and calculated analytically for both cases, is shown in Figs. 14(a) and 14(b). In the case of a heat conduction problem through a slab with a heat source (see Fig. 14(a)), the TMAP8 calculations are found to be in good agreement with the analytical solution, with RMSPE = 0.05%. Similarly, in the case of a heat conduction problem during a transient, the TMAP8 predictions match the analytical solution with RMSPE = 0.09% at  $t = 0.1$  s, RMSPE = 0.03% at  $t = 0.5$  s, RMSPE = 0.02% at  $t = 1$  s, and RMSPE = 0.00% at  $t = 5$  s (see Fig. 14(b)).

### 3.7. Ver-1g: Simple forward chemical reaction

#### 3.7.1. Case description

This verification problem is taken from Refs. [6,7]. A simple time-dependent chemical reaction given by



is modeled in a functional enclosure. The reaction rate,  $R$ , is positive if the species AB is being produced in the reaction and negative if it is being consumed. The forward rate coefficient,  $K$ , for the reaction has no spatial or time dependence. The reaction rate is

$$R = KC_A C_B, \quad (51)$$

where  $C_A$  and  $C_B$  are the concentrations of A and B, respectively. The reaction rate in terms of the concentrations of the reactants and product is given as

$$R = -\frac{d[C_A]}{dt} = -\frac{d[C_B]}{dt} = \frac{d[C_{AB}]}{dt} = KC_A C_B, \quad (52)$$

where  $C_{AB}$  is the concentration of species AB.

#### 3.7.2. Analytical solution

The analytical solution for the concentration of species AB as a function of time ( $t$ ) is given as

$$C_{AB} = C_{B_0} \frac{1 - \exp[Kt(C_{B_0} - C_{A_0})]}{1 - \frac{C_{B_0}}{C_{A_0}} \exp[Kt(C_{B_0} - C_{A_0})]}, \quad (53)$$

where  $C_{A_0}$  and  $C_{B_0}$  are the initial concentrations of A and B, respectively. For the special case when  $C_{A_0}$  and  $C_{B_0}$  are equal, Eq. (53)



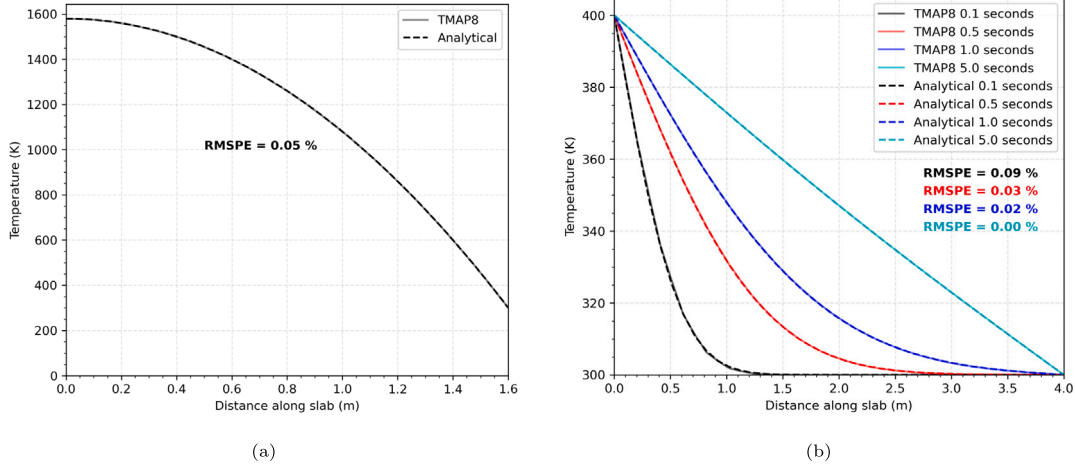


Fig. 14. (Ver-1f) Comparison of temperature along the slab calculated through TMAP8 and analytically for a heat conduction problem through a slab (a) with a heat source and (b) during a transient.

becomes

$$C_{AB} = C_{A_0} - \frac{1}{\frac{1}{C_{A_0}} + Kt}. \quad (54)$$

For this verification exercise, three cases were considered: (a) the initial concentrations of A and B are equal, (b) the initial concentrations of A and B are different and use the TMAP4 verification case values, and (c) the initial concentrations of A and B are different and use the TMAP7 verification case values. The equal concentration case is the same in TMAP4 and TMAP7 and is used for verification of TMAP8 here. While both TMAP4 and TMAP7 verification cases (b) and (c), respectively, have the same analytical solution, the different initial conditions produce different  $C_{AB}$  values over time, and we replicate both results here.

For case (a), the initial pressures of A and B were 1  $\mu\text{Pa}$ , and the reaction rate  $K$  is  $4.14 \times 10^3 \mu\text{m}^3/\text{atom s}$ . For case (b), the initial pressure of A was same as in case (a), while the initial pressure of B is 0.1  $\mu\text{Pa}$  as per TMAP4. For case (c), the initial pressure of A was same as in case (a), while the initial pressure of B is 0.5  $\mu\text{Pa}$ . In all cases, the initial pressures of A and B are first converted to their initial concentrations  $C_{A_0}$  and  $C_{B_0}$ , using the ideal gas law for the TMAP8 simulations and analytical solutions. The initial concentration  $C_{i_0}$  of component  $i$  is

$$C_{i_0} = 10^{-18} \frac{P_{i_0} N_a}{RT}, \quad (55)$$

where  $P_{i_0}$  is the initial pressure,  $N_a$  is Avogadro's constant,  $R$  is the gas constant, and  $T = 298.15 \text{ K}$  ( $25^\circ\text{C}$ ) is the temperature. The factor  $10^{-18}$  converts the concentration from atoms/ $\text{m}^3$  to atoms/ $\mu\text{m}^3$ .

### 3.7.3. Simulation results

A comparison of the concentration of AB as a function of time is plotted in Fig. 15(a) for case (a), and Fig. 15(b) for cases (b) and (c), respectively. The TMAP8 calculations are found to be in good agreement with the analytical solution with (a) RMSPE = 0.27%, (b) RMSPE = 0.22%, and (c) RMSPE = 0.24%, respectively.

## 3.8. Ver-1h: Convective gas outflow problem

### 3.8.1. Case description

This verification problem models a species ( $T_2$ , gaseous tritium) flowing through a system of three enclosures. It recreates the ver-1h case in Ref. [6] and ver-1ha in Ref. [7]. Gas flows from enclosure 1 into enclosure 2 and then from enclosure 2 into 3. Enclosure 1 is defined as

a boundary enclosure, so it is held at a constant pressure  $P_1$ , and the flow of gas into enclosures 2 and 3 can be given by

$$\bar{J}_i = QC_{i-1}, \quad (56)$$

where  $Q$  is the volumetric flow rate, and  $C_{i-1}$  is the concentration of gas molecules in the previous enclosure.

As gas flows through the system, the number of atoms of the gas entering the second and third enclosures is greater than the number exiting. The difference in pressures between two neighboring enclosures determines the net rate of gas flowing into the enclosure. The rate of change of the pressure of gas in the second and third enclosures is given as

$$\frac{P_2}{dt} = \frac{Q(P_1 - P_2)}{V_2}, \quad (57)$$

$$\frac{P_3}{dt} = \frac{Q(P_2 - P_3)}{V_3}. \quad (58)$$

We solve these time evolution equations for  $P_2$  and  $P_3$  using TMAP8 with  $t$  as the time and with the initial condition set to  $P_2 = P_3 = 0$ . We use  $V_2 = V_3 = 1 \text{ m}^3$ ,  $P_1 = 1.0 \text{ Pa}$ , and  $Q = 0.1 \text{ m}^3/\text{s}$ .

### 3.8.2. Analytical solution

The analytical solution to the equations Eqs. (57) and (58) is

$$P_2 = P_1 \left[ 1 - \exp\left(-\frac{Q}{V_2}t\right) \right], \quad (59)$$

and, if  $V_2 = V_3$ ,

$$P_3 = P_1 \left[ 1 - \left(1 + \frac{Q}{V_2}t\right) \exp\left(-\frac{Q}{V_2}t\right) \right]. \quad (60)$$

If  $V_2$  and  $V_3$  are not equal,

$$P_3 = P_1 \left[ 1 - \frac{V_2}{V_2 - V_3} \exp\left(-\frac{Q}{V_2}t\right) + \frac{V_3}{V_2 - V_3} \exp\left(-\frac{Q}{V_3}t\right) \right]. \quad (61)$$

In this analytical verification, we use the equal volume solution, Eq. (60), with the same values for the other parameters as used in the TMAP8 solution. Note that the TMAP4 verification case provides the initial value of  $P_1$ , but plots the solutions as gas concentrations instead, and only plots the solution up to 20 s [6]. The pressure calculations from TMAP8 and the analytical solutions are converted to concentration using the ideal gas law as

$$C_i = \frac{P_i N_a}{RT}, \quad (62)$$

where  $C_i$  is the concentration in atoms/ $\text{m}^3$ ,  $N_a$  is Avogadro's constant,  $R$  is the gas constant, and  $T = 303 \text{ K}$  is the temperature of the system [6].

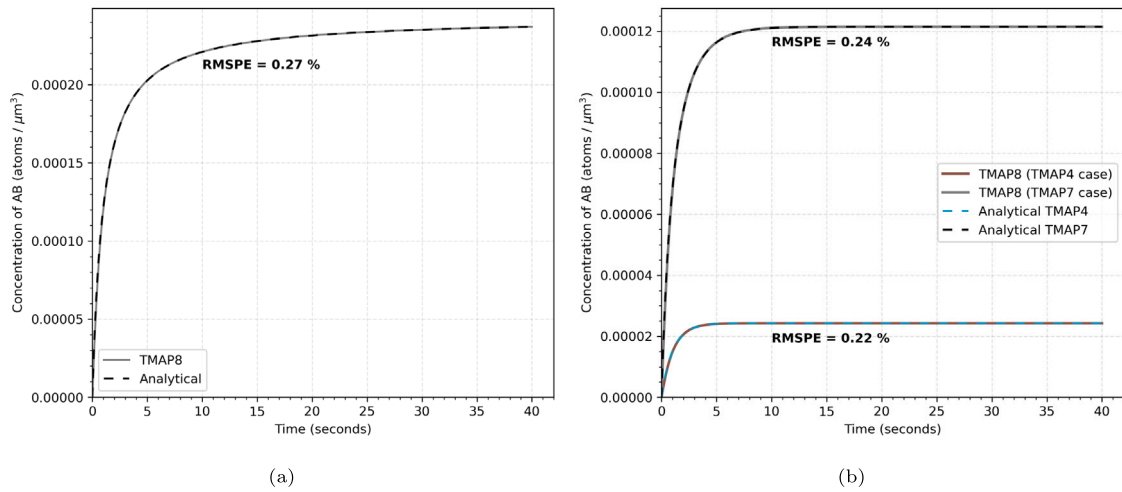


**Fig. 15.** (Ver-1g) Comparison of the concentration of AB as a function of time calculated through TMAP8 and analytically for the cases when (a) A and B have equal concentrations and (b) A and B have different concentrations. (b) shows comparisons for the initial conditions specified in both TMAP4, case (b), and TMAP7, case (c). TMAP8 predictions closely match the analytical solution in every condition.

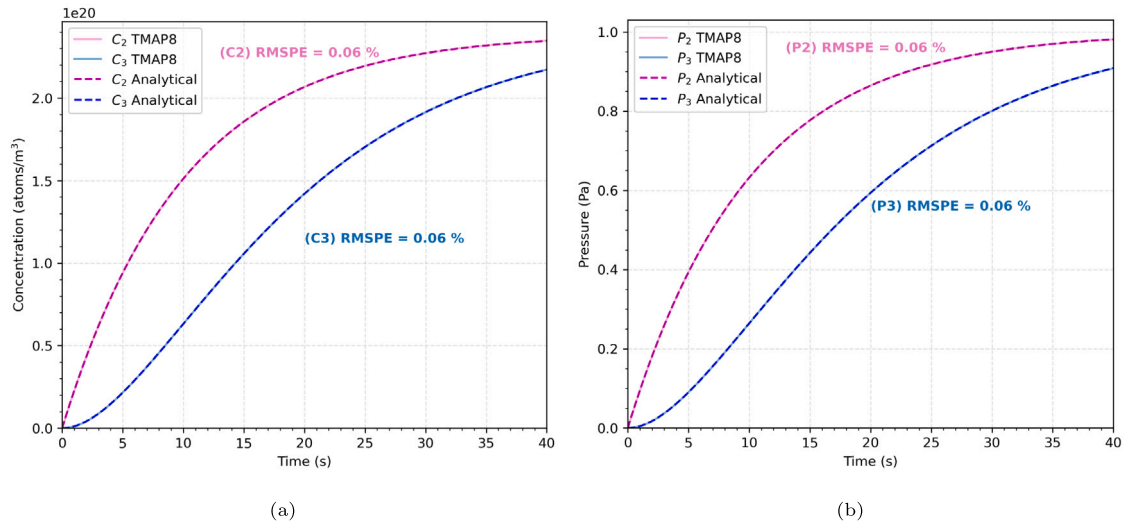


**Fig. 16.** (Ver-1h) Comparison of (a) concentration and (b) pressure of species  $T_2$  for the second and third enclosures in a series outflow predicted by TMAP8 and provided by the analytical solution. This recreates the verification figures from (a) TMAP4 [6] and (b) TMAP7 [7].

### 3.8.3. Simulation results

The comparison of TMAP8 results against the analytical solution is shown in Figs. 16(a) and 16(b). The match between TMAP8's predictions and the analytical solution is satisfactory, with RMSPE = 0.06% for both the 2nd and 3rd enclosures. The RMSPE value is the same for the concentration and pressure comparisons.

## 4. Validation of TMAP8 against experiments

Validation is the process of determining the degree to which a model accurately represents the real world for its intended uses, which requires comparison against experimental data [46]. In this section, we successfully compare TMAP8's predictions against experimental data for cases presented in Ref. [6] (i.e., val-2a, val-2b, and val-2c) with some updates from Ref. [7]. This demonstrates TMAP8's capability to model complex, real-life systems with high accuracy. Input files and scripts to reproduce the results and figures below are available at Ref. [10] and online in the TMAP8 documentation.

Because TMAP8's predictions are influenced by model parameter values with associated uncertainties, we use the STM available in MOOSE (and hence available in TMAP8) to calibrate the TMAP8 models

to better match the experimental data. Whenever relevant, both the non-calibrated and calibrated predictions are presented.

### 4.1. Val-2a: Ion implantation experiment

This validation problem is based on the data from Ref. [58], which describes an ion implantation experiment on a modified 316 stainless steel called Primary Candidate Alloy (PCA). This case is part of the validation suite of TMAP4 and TMAP7 as val-2a [6,7]. The PCA sample is a 0.5 mm thick disk with a diameter of 2.5 cm. It is exposed to a deuterium ion beam on the left side (also called the upstream side of the sample). The TRIM code [59] was used in Refs. [6,7] to determine that the average implantation depth for the ions is  $11 \text{ nm} \pm 5.4 \text{ nm}$ . Reemission data from the TRIM calculation shows that only 75% of the incident flux remained in the metal, and other 25% is re-emitted.

This model considers the diffusion in PCA and the recombination of deuterium on both sides. First, the diffusion of deuterium in PCA is described as

$$\frac{dC}{dt} = \nabla D \nabla C + S, \quad (63)$$

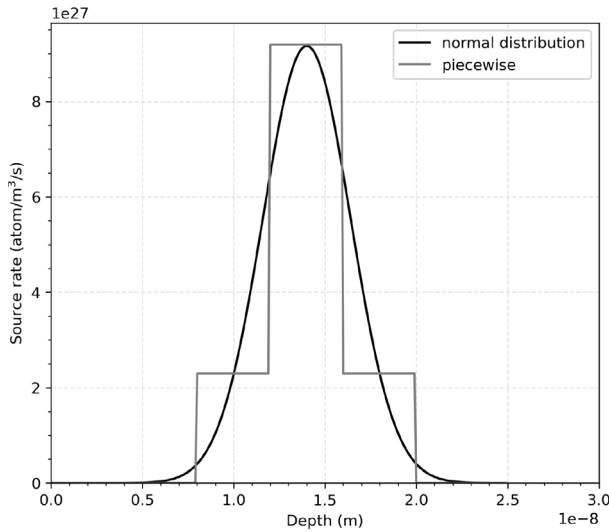


Fig. 17. (Val-2a) Comparison between the normal distribution from TMAP8 and the piecewise function from TMAP4 for the source term due to deuterium ion beam implantation.

where  $C$  is the concentration of deuterium in PCA,  $t$  is the time,  $D$  is the diffusivity of deuterium in PCA, and  $S$  is the source term in PCA due to the deuterium ion implantation.

Second, the deuterium recombines into gas on both sides of the PCA sample. By assuming that the recombination process is at steady state (which is not a necessary assumption in TMAP8, but appropriate in this case), it is described as the following surface flux

$$J = 2A(K_r C^2 - K_d P), \quad (64)$$

where  $J$  is the recombination flux out of the sample sides,  $A$  is the area on the upstream or downstream side,  $P$  is the pressure on the corresponding side, and  $K_r$  and  $K_d$  are the recombination and dissociation coefficients, respectively. The coefficient of 2 accounts for the fact that 2 deuterium atoms form one  $D_2$  molecule.

The objective of this simulation is to determine the permeation flux on the downstream side and match the experimental data published in Ref. [58] and reproduced in Fig. 18. In this case, TMAP8 simulates a 1D domain to represent the deuterium implantation, diffusion, and recombination. Note that this case can be easily extended to a 2D or 3D simulation.

The source term in the model is described as a normal distribution instead of the piecewise function from TMAP4 [6]. The source term of deuterium from ion beam implantation is defined as

$$S = F \frac{1.5}{\sigma \sqrt{2\pi}} \exp\left(-\frac{(x - \mu)^2}{2\sigma^2}\right), \quad (65)$$

where  $F$  is the implantation flux provided in Table 4,  $\sigma = 2.4 \times 10^{-9}$  m is the characteristic width of the normal distribution, and  $\mu = 14 \times 10^{-9}$  m is the depth of the normal distribution from the upstream side. Note that Eq. (65) uses the same factor of 1.5 from Ref. [6] to better correspond to implantation of experiment from Ref. [58]. The comparison between the normal distribution from TMAP8 and piecewise function from TMAP4 is shown in Fig. 17. The normal distribution has a similar distribution to the piecewise function, but the distribution profile is closer to the expected implantation profile.

The pressures on the upstream and downstream sides are close to vacuum pressures and have little impact for the recombination on both sides [6,7]. Thus, TMAP8 ignores the impact of pressure on the boundary conditions to simplify the model. The recombination is

Table 4

Values of beam flux on the upstream side of the sample during the experiment for val-2a [6,58].

Time (s)	Beam flux $F$ (atom/m <sup>2</sup> /s)
0–5820	$4.9 \times 10^{19}$
5820–9056	0
9056–12 062	$4.9 \times 10^{19}$
12 062–14 572	0
14 572–17 678	$4.9 \times 10^{19}$
17 678–20 000	0

Table 5

Values of material properties with  $f_i = (1 - 0.9999 \exp(-6 \times 10^{-5} t))$  (–) for val-2a. Note that  $K_r$  are currently not used in the input file since the upstream and downstream pressure do not noticeably influence the results.

Parameter	Value	Units	Reference
$K_d$ (upstream)	$8.959 \times 10^{18} f_i$	at/m <sup>2</sup> /s/Pa <sup>0.5</sup>	[6]
$K_d$ (downstream)	$1.7918 \times 10^{15}$	at/m <sup>2</sup> /s/Pa <sup>0.5</sup>	[6]
$K_r$ (upstream)	$1 \times 10^{-27} f_i$	m <sup>4</sup> /at/s	Inspired from [6]
$K_r$ (downstream)	$2 \times 10^{-31}$	m <sup>4</sup> /at/s	[58]
$P$ (upstream)	0	Pa	[58]
$P$ (downstream)	0	Pa	[58]
$D$	$3 \times 10^{-10}$	m <sup>2</sup> /2	[58]
$d$	0.025	m	[58]
$l$	$5 \times 10^{-4}$	m	[58]
$T$	703	K	[58]

described as a simplified version of Eq. (64),

$$J = 2AK_r C^2. \quad (66)$$

The beam flux on the upstream side of the sample during the experiment is presented in Table 4, and only 75% of the flux remains in the sample. Other case and model parameters used in TMAP8 are listed in Table 5. Note that the start and end times of the beam listed in Ref. [6] for TMAP8 are not accurate. Instead, TMAP8 uses the times directly from [58] to better correspond to experimental conditions. Both TMAP4 [6] and TMAP7 [7] describe the upstream recombination and dissociation coefficients as time-dependent exponentials rather than mechanistically capture the influence of ion irradiation on material performance. TMAP8 uses the same expressions.

TMAP4 [6] and TMAP7 [7] both replicate this validation case. However, they use different model parameters and configurations, and the experimental data presented in Ref. [7] for TMAP7 do not correspond to the data published in Ref. [58]. We therefore replicate only the data from TMAP4 and Ref. [58] in this TMAP8 validation case.

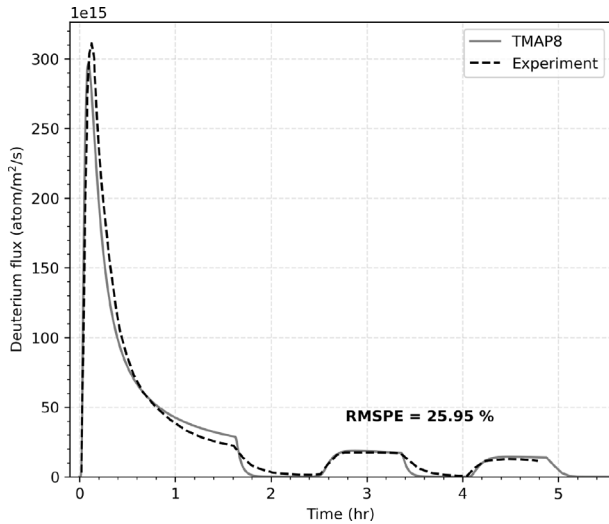
Fig. 18 shows the comparison of the TMAP8 calculation and the experimental data from Ref. [58]. There is reasonable agreement between the TMAP predictions and the experimental data with RMSPE = 25.95%. A preliminary effort to improve the match between TMAP8's prediction and the experimental data using the STM did not drastically reduce RMSPE. This suggests that the gap is not due to parameter values, but to experimental uncertainty and modeling inadequacy (i.e., limitations due to the model formulation, which might neglect contributions from key physics).

#### 4.2. Val-2b: Diffusion experiment in beryllium

This validation problem is taken from Ref. [60] and is part of the validation suite of TMAP4 and TMAP7 [6,7], which we reproduce here, with some updates. R.G. Macaulay-Newcombe et al. conducted thermal absorption and desorption experiments, as well as implantation experiments, on wafers of polished beryllium [60]. Of the several data sets presented, the one modeled here is titled “run 2a1” and is represented in Figure 2(a) in Ref. [60]. The beryllium sample was 0.4 mm thick and had an area of 104 mm<sup>2</sup>, as illustrated in Fig. 19. It was polished to a mirror finish and then exposed to 13.3 kPa of deuterium at 773 K for 50 h. It was quickly cooled under a vacuum of about 1  $\mu$ Pa. The

**Table 6**Model parameter values for the charging and the desorption phases in val-2b [6,7].  $T$  is the temperature in Kelvin.

Property of deuterium	Value for charging phase	Value for desorption phase	Units
Diffusivity in Be	$8.0 \times 10^{-9} \exp(-4220/T)$	$8.0 \times 10^{-9} \exp(-4220/T)$	$\text{m}^2/\text{s}$
Diffusivity in BeO	$1.40 \times 10^{-4} \exp(-24408/T)$	$7 \times 10^{-5} \exp(-27000/T)$	$\text{m}^2/\text{s}$
Solubility in Be	$7.156 \times 10^{27} \exp(-11606/T)$	$7.156 \times 10^{27} \exp(-11606/T)$	$\text{at}/\text{m}^3/\text{Pa}^{1/2}$
Solubility in BeO	$5.00 \times 10^{20} \exp(9377.7/T)$	$5.00 \times 10^{20} \exp(9377.7/T)$	$\text{at}/\text{m}^3/\text{Pa}^{1/2}$

**Fig. 18.** (Val-2a) Comparison of TMAP8 calculation with the experimental data from Ref. [58] on the downstream side of the sample. TMAP8 accurately replicates the experimental data.

cooling time constant for the apparatus is taken as 45 min, which is consistent with the assumption made in Refs. [6,7]. After removing the sample from the charging furnace, it was transferred in the air to a thermal desorption furnace, where the temperature was increased from ambient (300 K) to 1073 K at the rate of 3 K/min. This was done under vacuum, and the pressure of the chamber was monitored by the residual gas analysis and calibrated against standard leaks. In that way, the emission rate from the sample could be measured as a function of temperature. The sample pressure and temperature histories are shown in Fig. 20. Experimental data from that measurement, given in Figure 2 (a) in [60], are reproduced in Fig. 22.

The exact duration of the cooldown period and its temperature history are uncertain. Ref. [60] provides information about 24 hour-cooldown cycles, but it is unclear whether this applies to the charging chamber alone or to the sample as well. In parallel, Refs. [6,7] assume that the cooldown lasted for 40 min. With an assumed cooling time constant for the apparatus of 45 min, this did not enable the sample to cool down to the starting temperature of the desorption phase of the experiment (i.e., 300 K). To model this case in TMAP8, we decided to select a cooldown duration that is long enough to bring the temperature of the sample to around 300 K, but did not unnecessarily increase the length of the history since no significant changes happen to the deuterium distribution at 300 K due to slow kinetics. For these reasons, we selected a cooldown duration of 5 h, as shown in Fig. 20.

From Rutherford backscattering measurements made on the samples before charging with deuterium, it was deduced that the thickness of the oxide film was 18 nm. This is typical for polished beryllium. The metal is so reactive in air that the film forms almost immediately after any surface oxide removal. On the other hand, the oxide is relatively stable and would only grow slightly when exposed to air between charging and thermal desorption.

This experiment is modeled using a two-segment model in TMAP8 with the segments linked. The first segment is the beryllium oxide

(BeO) film, which is modeled using 18 elements, each 1 nm in length. The second segment is the beryllium with reflective boundary condition at the mid-plane. The beryllium segment is modeled using 40 elements, each 50  $\mu\text{m}$  thick. The solubility of deuterium in beryllium used was that given by Refs. [61,62].

The materials properties used in this study are inspired from the ones used in Refs. [6,7]. The diffusivity of deuterium in beryllium is taken from Ref. [63], where the authors made measurements on high-grade (99% pure) and extra-grade (99.8% pure), consistent with Macaulay-Newcombe's measurements of the purity of his samples [60].

The authors of Refs. [6,7] expressed less certainty about the material property values used for BeO, in part because it is not clear in which state the deuterium exists in the BeO. Refs. [6,7] use a value close to  $-78.8 \text{ kJ/mol}$  (exothermic solution) and justify it using the values and analysis from. In this study, we use the same value as Refs. [6,7] ( $-9377.7 \text{ K}$ ) while recognizing its large uncertainty [5,64]. For deuterium solubility in BeO, Refs. [6,7] used  $5 \times 10^{20} \text{ d}/\text{m}^3 \text{ Pa}^{1/2}$ , which, given the large uncertainties, is not too far from the value of  $1.88 \times 10^{18} \text{ d}/\text{m}^3 \text{ Pa}^{1/2}$  inferred from measurements of 200 appm of D in BeO after exposure to 13.3 kPa of  $\text{D}_2$  at 773 K extracted from Ref. [65] and alleged follow-up conversations. Deuterium diffusion measurements in BeO were obtained from Ref. [66], which measured it for single-crystal, sintered, and powdered BeO and quantified microstructural effects on deuterium diffusivity. The model in Refs. [6,7] uses one expression for the charging phase and another for the thermal desorption phase, believing that the surface film changed somewhat during the transfer between the two furnaces. For the charging phase diffusivity, the model uses 20 times that for the sintered BeO. Thermal expansion mismatches tend to open up cracks and channels in the oxide layer, so this seems a reasonable value. The same activation energy of 48.5 kJ/mol is retained, however. For the thermal desorption phase, the diffusivity prefactor of the sintered material ( $7 \times 10^{-5} \text{ m}^2/\text{s}$ ) and an activation energy of 223.7 kJ/mol (53.45 kcal/mol) are used. These values give results lying well within the scatter of Fowler's data. Exposure of the sample to air after heating should have made the oxide more like a single crystal by healing the cracks that may have developed. Diffusivities and solubilities used in the simulation are listed in Table 6.

The model applies 13.3 kPa of  $\text{D}_2$  for 50 h and 15 s followed by cool down with a 45 min time constant at  $1 \mu\text{Pa}$  for 5 h [6,7] used 40 min, but we extend it here to 5 h to let the temperature go down closer to 300 K—see Fig. 20. The deuterium concentrations in the sample have a complex distribution that results from first charging the sample and then discharging it during the cooldown. This problem is then restarted with different model parameters (see Table 6) to simulate thermal desorption in a  $1 \times 10^{-3} \text{ Pa}$  environment that begins at 300 K and goes to 1073 K at 3 K/min.

The experimental data used in this case comes directly from Figure (2) in Ref. [60]. This is in contrast with the data used in Refs. [6, 7], which, although the scale of the data is very similar, differs slightly. Also, note that the units in Figure (2) from [60] should be  $\text{atoms}/\text{mm}^2/\text{s} \times 10^{10}$  instead of  $\text{atoms}/\text{mm}^2 \times 10^{10}$ , which is corrected in Fig. 22.

To verify that the solubility ratio at the interface between the beryllium and its oxide is appropriately modeled, Fig. 21 compares the known solubility ratio with the calculated deuterium concentration ratio at the interface, and they match, as expected.



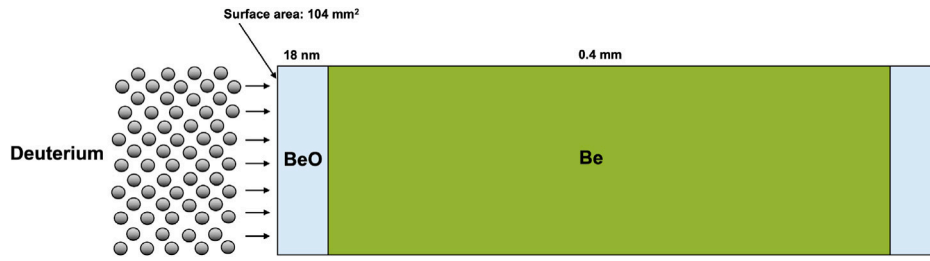


Fig. 19. Schematic of the experiment setup for Val-2b (figure elements are not to scale).

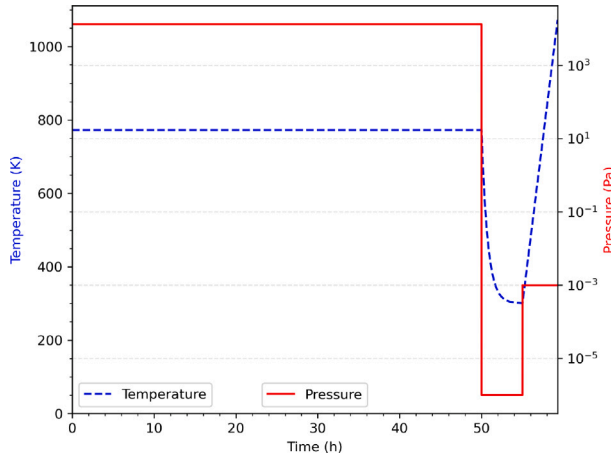


Fig. 20. Pressure and temperature histories for Val-2b.

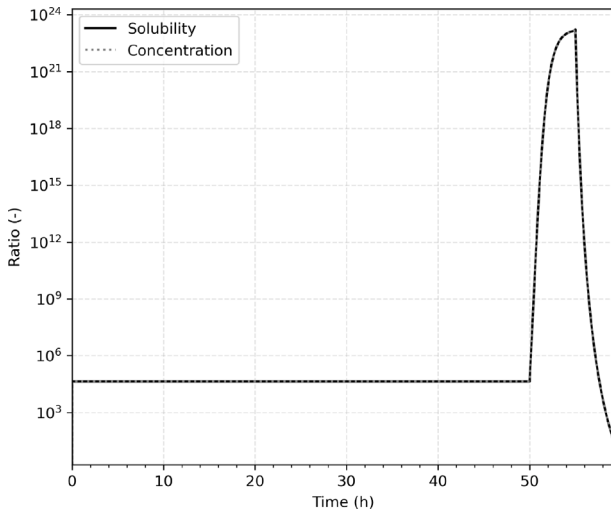


Fig. 21. (Val-2b) Solubility and concentration ratio at the Be-BeO interface. The match shows that the solubility difference is properly enforced in TMAP8.

In TMAP4 and TMAP7, this case was divided in two simulations to accommodate the different model parameters used during charging and desorption (see Table 6) [6,7]. In TMAP8, the full history is modeled in one simulation.

Fig. 22 compares the TMAP8 calculation with experimental data during the desorption process. There is reasonable agreement between the TMAP predictions and the experimental data, with a RMSPE of 22.72%. While the TMAP8 calculation accurately captures the temperature at which the flux peaks, the magnitude of the peak deuterium flux is underestimated. Given the aforementioned uncertainties in diffusivities and solubilities for Be and BeO, parameter calibration is performed

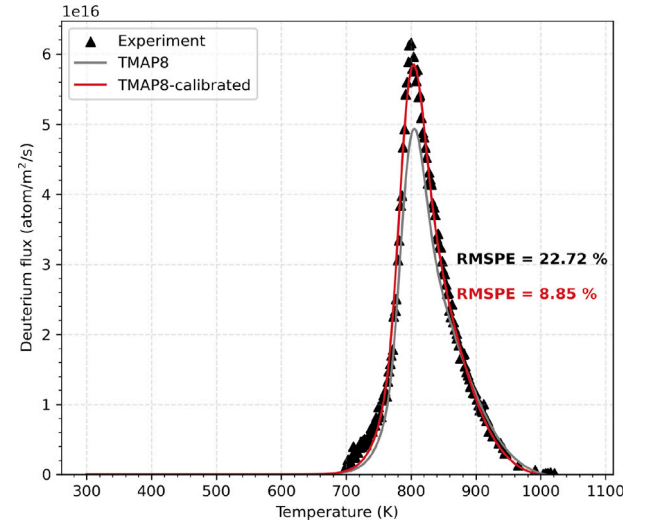


Fig. 22. (Val-2b) Comparison of TMAP8 calculation against experimental data during desorption [60], which shows TMAP8's ability to accurately model this diffusion experiment.

leveraging the MOOSE STM to minimize the discrepancy between the TMAP8 prediction and experimental measurements. It is also shown in Fig. 22 that the RMSPE decreases to 8.85% after calibration, resulting in significantly improved agreement with the experimental data.

When calibrating the model parameters, we utilized the subset simulation algorithm (through the ParallelSubsetSimulation sampler) in MOOSE STM. Subset simulation is a stochastic optimization algorithm that iteratively proposes Markov chain samples to maximize the objective function [67]. The parallel implementation of the subset simulation algorithm within the MOOSE framework enables the efficient proposal of new samples across multiple Markov chains, which are simulated in parallel [68]. In this case, the objective is defined as the reciprocal of the time integral of flux differences between the TMAP8 simulation and experimental data. During the subset simulation, this objective function is maximized. The calibrated model parameters, assuming identical values for deuterium diffusivity in Be, deuterium solubility in Be, and deuterium solubility in BeO during both the charging phase and desorption phases (only the diffusivity in BeO is different), are shown in Table 7. The TMAP8 simulation, using these calibrated parameters, is represented by the red curve in Fig. 22, which shows a much improved alignment with the experimental data, particularly at the flux peak, and a reduced RMSPE.

#### 4.3. Val-2c: Test cell experiment

This validation problem is taken from Ref. [69] and was part of the validation suite of TMAP4 [6] and TMAP7 [7]. Whenever tritium is released into a fusion reactor test cell, it is crucial to clean it up to prevent exposure. This case models an experiment conducted at Los

Table 7

Calibrated model parameter values for the charging and the desorption phases in val-2b.  $T$  is the temperature in Kelvin.

Property of deuterium	Calibrated value for charging phase	Calibrated value for desorption phase	Units
Diffusivity in Be	$7.950 \times 10^{-9} \exp(-4145.609/T)$	Identical	$\text{m}^2/\text{s}$
Diffusivity in BeO	$1.402 \times 10^{-4} \exp(-24542.561/T)$	$6.949 \times 10^{-5} \exp(-26941.820/T)$	$\text{m}^2/\text{s}$
Solubility in Be	$7.072 \times 10^{27} \exp(-11623.038/T)$	Identical	$\text{at}/\text{m}^3/\text{Pa}^{1/2}$
Solubility in BeO	$5.005 \times 10^{20} \exp(9446.043/T)$	Identical	$\text{at}/\text{m}^3/\text{Pa}^{1/2}$

Alamos National Laboratory at the tritium systems test assembly to study the behavior of tritium once released in a test cell and the efficacy of the emergency tritium cleanup system.

The experimental setup, described in greater detail in Ref. [69], can be summarized as the inner walls of an enclosure of volume  $V$  are covered with an aluminum foil and then covered in paint with an average thickness  $l$ , which is then in contact with the enclosure air. A given amount,  $T_2^0$ , of tritium,  $T_2$ , is injected in the enclosure, which initially contained ambient air, representing the tritium release. A flow rate  $f$  through the enclosure represents the air replacement time expected for large test cells. The purge gas is ambient air with 20% relative humidity. A fraction of that amount is diverted through the measurement system to determine the concentrations of chemical species within the enclosure.

Several phenomena are taking place and need to be captured in the model to determine the concentrations of elemental tritium (i.e.,  $T_2$  and HT), tritiated water (i.e., HTO), and water (i.e.,  $H_2O$ ). First, The following chemical reactions occur inside the enclosure



mostly as a consequence of the tritium reactivity. The reaction rates of these reactions are  $K_1$  and  $K_2$ , respectively, where

$$K_1 = 2K^0 c_{T_2} (2c_{T_2} + c_{\text{HT}} + c_{\text{HTO}}) \quad (69)$$

and

$$K_2 = K^0 c_{\text{HT}} (2c_{T_2} + c_{\text{HT}} + c_{\text{HTO}}). \quad (70)$$

Here,  $c_i$  represents the concentration of species  $i$ , and  $K^0$  is a constant.

Second, the different species will permeate in the paint. The elemental tritium species,  $T_2$  and HT, have a given solubility  $K_S^e$  and diffusivity  $D^e$ , while the tritiated water, HTO, and water,  $H_2O$ , have a solubility  $K_S^w$  and diffusivity  $D^w$ . It is expected that the species will initially permeate into the paint and later get released as the purge gas cleans up the enclosure air.

The objectives of this case are to determine the time evolution of  $T_2$  and HTO concentrations in the enclosure, match the experimental data published in Ref. [69], and display this comparison with the appropriate error checking (see Figs. 23(a) and 23(b)).

To model the case described above, TMAP8 simulates a 1D domain with one block to represent the air in the enclosure and another block to represent the paint. In each block, the simulation tracks the local concentration of  $T_2$ , HT, HTO, and  $H_2O$ . Note that this case can easily be extended to a 2D or 3D case, but consistent with previous analyses, we will maintain the 1D configuration here.

In the enclosure, to capture the purge gas and the chemical reactions, the concentrations evolve as

$$\frac{dc_{T_2}}{dt} = -K_1 - \frac{f}{V} c_{T_2}, \quad (71)$$

$$\frac{dc_{\text{HT}}}{dt} = K_1 - K_2 - \frac{f}{V} c_{\text{HT}}, \quad (72)$$

$$\frac{dc_{\text{HTO}}}{dt} = K_1 + K_2 - \frac{f}{V} c_{\text{HTO}}, \quad (73)$$

and

$$\frac{dc_{H_2O}}{dt} = -K_1 - K_2 + \frac{f}{V} (c_{H_2O}^0 - c_{H_2O}), \quad (74)$$

where  $c_{H_2O}^0$  is the concentration of  $H_2O$  in the incoming purge gas.

In the paint, TMAP8 captures species diffusion through

$$\frac{dc_{T_2}}{dt} = \nabla D^e \nabla c_{T_2}, \quad (75)$$

$$\frac{dc_{\text{HT}}}{dt} = \nabla D^e \nabla c_{\text{HT}}, \quad (76)$$

$$\frac{dc_{\text{HTO}}}{dt} = \nabla D^w \nabla c_{\text{HTO}}, \quad (77)$$

and

$$\frac{dc_{H_2O}}{dt} = \nabla D^w \nabla c_{H_2O}. \quad (78)$$

At the interface between the enclosure air and the paint, sorption is captured in TMAP8 with Henry's law

$$c_{i,\text{enclosure}} = K_S c_{i,\text{paint}} RT, \quad (79)$$

where  $c_{i,\text{enclosure}}$  and  $c_{i,\text{paint}}$  are the concentrations of species  $i$  in the enclosure and in the paint, respectively, and  $K_S$  is the solubility (either  $K_S^e$  or  $K_S^w$ ). The boundary conditions are set to "no flux" since no permeation happens at the interface between the paint and the aluminum foil, and the only flux leaving the enclosure is captured by the purge gas [69].

One of the assumptions made in the original paper and TMAP4 V&V case is that the tritium is immediately added to the enclosure [6,69]. However, this leads to an early HTO peak concentration, which does not exactly match the experimental data. In Ref. [7], TMAP7 introduces a new enclosure to account for a slower injection of tritium. Here, we model this case with two different approaches. The first approach, like Refs. [6,69], assumes that the entire tritium inventory is immediately injected in the enclosure at the beginning of the experiment. The second approach assumes that the tritium inventory is being injected into the enclosure at a linear rate during a period of time  $t_{\text{injection}}$  until the entire tritium inventory is injected. The results of these two approaches are presented and discussed below.

The case and model parameters used in both approaches in TMAP8 are listed in Table 8. Some of the parameters are directly leveraged from Refs. [6,7,69], but others were adapted to better match the experimental data.

Figs. 23(a) and 23(b) show the comparison of the TMAP8 calculations (both with immediately injected and delayed injected  $T_2$ ) against the experimental data for  $T_2$  and HTO concentration in the enclosure over time. There is reasonable agreement between the TMAP8 predictions and the experimental data. In the case of immediate  $T_2$  injection, the RMSPEs are equal to RMSPE = 58.98% for  $T_2$  and RMSPE = 139.10% for HTO, respectively. When accounting for a delay in  $T_2$  injection, the TMAP8 predictions better match the experimental data, in particular the position of the peak HTO concentration. The RMSPE values decrease to RMSPE = 58.05% for  $T_2$  and RMSPE = 74.77% for HTO, respectively. Note that the model parameters listed in Table 8 are somewhat different from Refs. [6,7,69] to better match the experimental data. In particular, Refs. [6,7] did not validate the TMAP

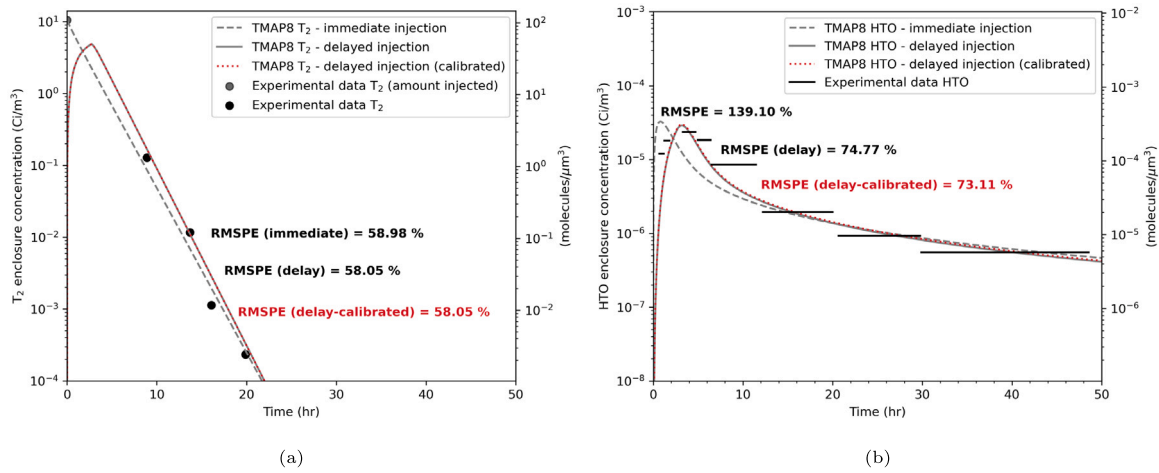


Fig. 23. (Val-2c) Comparison of TMAP8 calculations against the experimental data from a test cell experiment. (a) T<sub>2</sub> concentration in the enclosure over time. (b) HTO concentration in the enclosure over time. TMAP8 matches the experimental data well, with an improvement when T<sub>2</sub> is injected over a given period rather than immediately.

Table 8

Case and model parameters values used in both approaches in TMAP8 for val-2c. When values are the same for both approaches, they are noted as identical. Model parameters that have been adapted from Ref. [6] show a corrective factor in bold.

Parameter	Immediate injection approach	Delayed injection approach	Unit	Reference
$V$	0.96	Identical	m <sup>3</sup>	[69]
$l$	0.16 (between 0.1 and 0.2)	Identical	mm	[69]
$T_2^0$	10	Identical	Ci/m <sup>3</sup>	[69]
$c_{H_2O}^0$	714	Identical	Pa	[6]
$f$	0.54	Identical	m <sup>3</sup> /h	[69]
$T$	303	Identical	K	[69]
Total time	180 000	Identical	s	[69]
$K^0$	$1.5 \times 2.0 \times 10^{-10}$	$2.8 \times 2.0 \times 10^{-10}$	m <sup>3</sup> /Ci/s	Adapted from [6]
$D^e$	$4.0 \times 10^{-12}$	Identical	m <sup>2</sup> /s	[69]
$D^w$	$1.0 \times 10^{-14}$	Identical	m <sup>2</sup> /s	[69]
$K_S^e$	$5.0 \times 10^{-2} \times 4.0 \times 10^{19}$	$1.0 \times 10^{-3} \times 4.0 \times 10^{19}$	1/m <sup>3</sup> /Pa	Adapted from [6]
$K_S^w$	$3.5 \times 10^{-4} \times 6.0 \times 10^{24}$	$3.0 \times 10^{-4} \times 6.0 \times 10^{24}$	1/m <sup>3</sup> /Pa	Adapted from [6]
$t_{injection}$	N/A	3	h	

predictions against T<sub>2</sub> concentration, which we do here in Fig. 23(a). This affects some of the model parameters.

The agreement between modeling predictions and experimental data is modestly improved by calibrating the model parameters. The optimization is again performed using MOOSE STM with the subset simulation sampler, assuming delayed tritium injection. The calibrated parameters include  $K^0$ ,  $D^e$ ,  $D^w$ ,  $K_S^e$ ,  $K_S^w$ , and  $t_{injection}$ . Unlike the previous case, the optimization here is multi-objective, aiming to minimize the time integral difference between the experimental data and TMAP8 simulations for both the T<sub>2</sub> and HTO concentrations (adopting a weighted sum of the two integral differences). Notably, the integral difference is defined in logarithmic space to give equal weight to all data points in the logarithmic scale during the optimization process.

As shown in the red curve in Fig. 23, the overall agreement with the experimental data improves slightly after calibration. The RMSPE for HTO slightly decreases from 74.77% to 73.11%, while the calibrated result has little impact on T<sub>2</sub> predictions, with the RMSPE remaining at 58.05%. The comparison between the original and calibrated values of selected model parameters is summarized in Table 9, with  $K_S^e$  showing the most significant update during the optimization, which does not seem to greatly affect the model predictions due to its low sensitivity.

## 5. Integrated fuel cycle capabilities

TMAP8 has the capacity to model the tritium fuel cycle on a system level. We demonstrate this by recreating the model described in Ref. [70]. In the referenced work, eleven systems work in conjunction to describe the tritium life-cycle of a fusion device. The equations are listed in Table 10.

Table 9

Calibrated model parameters values for the delayed injection case in val-2c.

Parameter	Original value	Calibrated value	Unit
$K^0$	$2.8 \times 2.0 \times 10^{-10}$	$2.891 \times 2.0 \times 10^{-10}$	m <sup>3</sup> /Ci/s
$D^e$	$4.0 \times 10^{-12}$	$3.997 \times 10^{-12}$	m <sup>2</sup> /s
$D^w$	$1.0 \times 10^{-14}$	$0.965 \times 10^{-14}$	m <sup>2</sup> /s
$K_S^e$	$1.0 \times 10^{-3} \times 4.0 \times 10^{19}$	$1.885 \times 10^{-2} \times 4.0 \times 10^{19}$	1/m <sup>3</sup> /Pa
$K_S^w$	$3.0 \times 10^{-4} \times 6.0 \times 10^{24}$	$3.533 \times 10^{-4} \times 6.0 \times 10^{24}$	1/m <sup>3</sup> /Pa
$t_{injection}$	3	3.096	h

Table 10

System of equations used in the TMAP8 tritium fuel-cycle example model.

System name	System number	System equation
Breeding zone	1	(80)
Tritium extraction system	2	(81)
First wall	3	(82)
Divertor	4	(83)
Heat exchanger	5	(84)
Coolant purification system	6	(85)
Vacuum pump	7	(86)
Fuel clean-up	8	(87)
Isotope separation system	9	(88)
Exhaust and water detritiation system	10	(89)
Storage and management	11	(90)

The TMAP8 model of the system is made by defining “scalar” variables. In MOOSE-based modeling, these differ from field variables in that they are defined by a single value, instead of being discretized over

a field. This allows for more computational efficiency. Each of the variables is coupled to the others through objects called “ScalarKernels”, with the time-dependent terms defined using “ODETimeDerivative” objects and the rest defined using “ParsedODEKernel” objects. The system of equations (see Eqs. (80)–(90)) are internally represented with all terms on the left of the equality, but are presented here in standard form.

$$\frac{dI_1}{dt} = \Lambda \dot{N}^- + (1 - \eta_2) \frac{I_2}{\tau_2} - \frac{I_1}{\tau_1} - \frac{I_1 \epsilon_1}{\tau_1} - I_1 \lambda, \quad (80)$$

$$\frac{dI_2}{dt} = (1 - f_{1-5}) \frac{I_1}{\tau_1} - \frac{I_2}{\tau_2} - \frac{I_2 \epsilon_2}{\tau_2} - I_2 \lambda, \quad (81)$$

$$\begin{aligned} \frac{dI_3}{dt} = & f_{p-3} \frac{\dot{N}^-}{\eta_f f_b} + f_{5-3}(1 - f_{5-6})(1 - f_{5-10}) \frac{I_5}{\tau_5} + f_{6-3}(1 - \eta_6) \frac{I_6}{\tau_6} \\ & - \frac{I_3}{\tau_3} - \frac{I_3 \epsilon_3}{\tau_3} - I_3 \lambda, \end{aligned} \quad (82)$$

$$\begin{aligned} \frac{dI_4}{dt} = & f_{p-4} \frac{\dot{N}^-}{\eta_f f_b} + (1 - f_{5-3})(1 - f_{5-6})(1 - f_{5-10}) \frac{I_5}{\tau_5} \\ & + (1 - f_{6-3})(1 - \eta_6) \frac{I_6}{\tau_6} - \frac{I_4}{\tau_4} - \frac{I_4 \epsilon_4}{\tau_4} - I_4 \lambda, \end{aligned} \quad (83)$$

$$\frac{dI_5}{dt} = f_{1-5} \frac{I_1}{\tau_1} + \frac{I_3}{\tau_3} + \frac{I_4}{\tau_4} - \frac{I_5}{\tau_5} - \frac{I_5 \epsilon_5}{\tau_5} - I_5 \lambda, \quad (84)$$

$$\frac{dI_6}{dt} = f_{5-6}(1 - f_{5-10}) \frac{I_5}{\tau_5} - \frac{I_6}{\tau_6} - \frac{I_6 \epsilon_6}{\tau_6} - I_6 \lambda, \quad (85)$$

$$\frac{dI_7}{dt} = (1 - \eta_f f_b - f_{p-3} - f_{p-4}) \frac{\dot{N}^-}{\eta_f f_b} - \frac{I_7}{\tau_7} - \frac{I_7 \epsilon_7}{\tau_7} - I_7 \lambda, \quad (86)$$

$$\frac{dI_8}{dt} = \frac{I_7}{\tau_7} - \frac{I_8}{\tau_8} - \frac{I_8 \epsilon_8}{\tau_8} - I_8 \lambda, \quad (87)$$

$$\frac{dI_9}{dt} = (1 - f_{8-11}) \frac{I_8}{\tau_8} + \frac{I_{10}}{\tau_{10}} + \eta_2 \frac{I_2}{\tau_2} + \eta_6 \frac{I_6}{\tau_6} - \frac{I_9 \epsilon_9}{\tau_9} - \frac{I_9}{\tau_9} - I_9 \lambda, \quad (88)$$

$$\frac{dI_{10}}{dt} = f_{5-10} \frac{I_5}{\tau_5} + f_{9-10} \frac{I_9}{\tau_9} - \frac{I_{10}}{\tau_{10}} - \frac{I_{10} \epsilon_{10}}{\tau_{10}} - I_{10} \lambda, \quad (89)$$

and

$$\frac{dI_{11}}{dt} = f_{8-11} \frac{I_8}{\tau_8} + (1 - f_{9-10}) \frac{I_9}{\tau_9} - \frac{\dot{N}^-}{\eta_f f_b} - I_{11} \lambda. \quad (90)$$

To facilitate the modular nature of TMAP8, the system parameters are modeled using postprocessors, which could be controlled through the STM or could be replaced with sub-models that accurately calculate the relevant parameter.

In order to compare with previously published literature results, we assume specific values for several parameters in our model. We start with a system failure fraction  $q$  of 0.25 and an operational reserve time of 1 d. This leads to a minimum reserve inventory of 127.5 kg. Vacuum pump and fuel clean-up system residence times  $\tau_7$  and  $\tau_8$  are both set to 1 s, and given the reserve inventory and the constraint of a 5-year doubling time, the tritium breeding ratio  $\Lambda$  is set to 1.9247 by trial-and-error. The initial value of tritium in storage  $I_{11}$  is 225.4215 kg. As shown in Fig. 24, the agreement between the results of this work and those from extrapolation of Figure 3 in [70] is within the margin of error associated with reading the figure. Detailed RMSPE calculations were not carried out in this case.

The full source code, a detailed model explanation, and a graphical model interface of the fuel cycle model are available online as discussed in Data Availability section.

## 6. Conclusion and future work

Given how crucial tritium management is for the safety, sustainability, and economics of fusion energy systems, the need for trusted advanced modeling and simulations capabilities to accelerate tritium

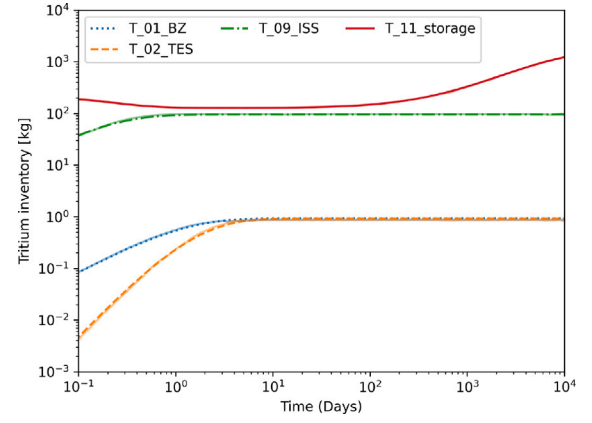


Fig. 24. Tritium inventories of specific systems as a function of time. Dashed lines are best estimate of Figure 3 in Ref. [70], and solid lines represent TMAP8 results.

technology development and deployment is evident. TMAP8 is being developed as an open-source, multiscale (from the mesoscale to component- and system-level) advanced modeling and simulation tool following high SQA standards for reliable safety and design studies.

In this publication, we introduce the MOOSE-based TMAP8 application and describe some of its key attributes and features supporting the burgeoning fusion industry: its openness for transparency and accessibility, its SQA and software development practices for reliability, repeatability, and applicability to safety assessment and design studies, and its modularity and ability to couple with other MOOSE-based tools for multiphysics applications. In particular, this paper presents the current state of the V&V cases suite matching those in TMAP4, including calibration of TMAP8’s predictions against experimental data using the integrated stochastic capabilities available in MOOSE. This not only highlights existing TMAP8 capabilities for tritium transport and heat transfer modeling but also provides an open and reproducible database of V&V cases that can be utilized (1) as a way to exercise TMAP8, (2) as starting points for new users, and (3) as a source of V&V and benchmarking cases for other tritium modeling tools. This paper also presents current fuel cycle capabilities in TMAP8, which highlight TMAP8’s flexibility in scale.

Future work will focus on expanding the V&V case suite to match those used in TMAP7 [7] and expand it using more recent experimental data. In parallel, TMAP8’s coupling with FENIX for multiphysics simulations will explore the impact of the interactions between different physics and different scales on tritium transport [24,43]. The list of physics being coupled with TMAP8 will increase to address the evolving needs of the industry.

## CRedit authorship contribution statement

**Pierre-Clément A. Simon:** Writing – original draft, Validation, Supervision, Software, Project administration, Conceptualization, Funding acquisition. **Casey T. Icenhour:** Writing – original draft, Validation, Software, Conceptualization, Funding acquisition. **Gyanender Singh:** Writing – review & editing, Validation, Software. **Alexander D. Lindsay:** Writing – review & editing, Validation, Software. **Chaitanya Bhawe:** Writing – review & editing, Validation, Software. **Lin Yang:** Writing – review & editing, Validation, Software. **Adriaan Riet:** Writing – review & editing, Validation, Software. **Yifeng Che:** Writing – review & editing, Validation. **Paul Humrickhouse:** Writing – review & editing, Supervision, Software, Funding acquisition, Conceptualization. **Patrick Calderoni:** Writing – review & editing. **Masashi Shimada:** Writing – review & editing, Supervision, Project administration, Funding acquisition, Conceptualization.



## Declaration of competing interest

The authors declare that they have no known competing financial interests or personal relationships that could have appeared to influence the work reported in this paper.

## Acknowledgments

This work was supported by the U.S. Department of Energy, Office of Science, Office of Fusion Energy Sciences, and authored by Battelle Energy Alliance, LLC under Contract No. DE-AC07-05ID14517. This work was also supported through INL's Laboratory Directed Research & Development (LDRD), United States Program under DOE Idaho Operations Office Contract DE-AC07-05ID14517. The United States Government retains, and the publisher, by accepting the article for publication, acknowledges that the United States Government retains a nonexclusive, paid-up, irrevocable, worldwide license to publish or reproduce the published form of this manuscript, or allow others to do so, for United States Government purposes.

This research made use of the resources of the High Performance Computing Center at Idaho National Laboratory, which is supported by the Office of Nuclear Energy of the U.S. Department of Energy and the Nuclear Science User Facilities, United States under Contract No. DE-AC07-05ID14517.

## Appendix. Derivation of the weak form of the equations from ver-1d

The derivation of the weak form from the strong form of the equations follows five main steps. In this section, we detail these steps for the coupled diffusion and trapping equations described in Section 3.4.3 for case ver-1d with multiple trapping sites.

### A.1. Step 1: Define and rearrange the strong form of the equations

The strong form of the governing equations is provided in Eqs. (28) and (29), and can be slightly rearranged as:

$$\frac{\partial C_M}{\partial t} - \nabla \cdot (D \nabla C_M) + \text{trap\_per\_free} \cdot \sum_{i=1}^3 \frac{\partial C_{T_i}}{\partial t} = 0, \quad (\text{A.1})$$

and, for  $i = 1, i = 2$ , and  $i = 3$ :

$$\frac{\partial C_{T_i}}{\partial t} - \alpha_i^i \frac{C_{T_i}^{\text{empty}} C_M}{N \cdot \text{trap\_per\_free}} + \alpha_r^i C_{T_i} = 0, \quad (\text{A.2})$$

respectively.

### A.2. Step 2: Multiply every term by a test function

Multiply each term of the equations by an appropriate test function  $\psi$  (or  $\psi_i$  for  $C_{T_i}$ ). Eq. (A.1) becomes

$$\psi \frac{\partial C_M}{\partial t} - \psi \nabla \cdot (D \nabla C_M) + \psi \cdot \text{trap\_per\_free} \cdot \sum_{i=1}^3 \frac{\partial C_{T_i}}{\partial t} = 0, \quad (\text{A.3})$$

and, for  $i = 1, i = 2$ , and  $i = 3$ , Eq. (A.2) becomes

$$\psi_i \left( \frac{\partial C_{T_i}}{\partial t} - \alpha_i^i \frac{C_{T_i}^{\text{empty}} C_M}{N \cdot \text{trap\_per\_free}} + \alpha_r^i C_{T_i} \right) = 0. \quad (\text{A.4})$$

### A.3. Step 3: Integrate over the domain $\Omega$

After integration over the domain, we obtain:

$$\int_{\Omega} \psi \frac{\partial C_M}{\partial t} d\Omega - \int_{\Omega} \psi \nabla \cdot (D \nabla C_M) d\Omega + \int_{\Omega} \psi \cdot \text{trap\_per\_free} \cdot \sum_{i=1}^3 \frac{\partial C_{T_i}}{\partial t} d\Omega = 0, \quad (\text{A.5})$$

and, for  $i = 1, i = 2$ , and  $i = 3$ ,

$$\int_{\Omega} \psi_i \frac{\partial C_{T_i}}{\partial t} d\Omega - \int_{\Omega} \psi_i \alpha_i^i \frac{C_{T_i}^{\text{empty}} C_M}{N \cdot \text{trap\_per\_free}} d\Omega + \int_{\Omega} \psi_i \alpha_r^i C_{T_i} d\Omega = 0. \quad (\text{A.6})$$

### A.4. Step 4: Integrate by parts and apply the divergence theorem

For the divergence term in Eq. (A.5), applying integration by parts and the divergence theorem provides

$$\int_{\Omega} \psi \nabla \cdot (D \nabla C_M) d\Omega = - \int_{\Omega} \nabla \psi \cdot (D \nabla C_M) d\Omega + \oint_{\partial\Omega} \psi (D \nabla C_M) \cdot \mathbf{n} d\partial\Omega, \quad (\text{A.7})$$

where  $\partial\Omega$  is the boundary of the domain and  $\mathbf{n}$  is the outward-facing normal vector.

This update term is then substituted back into Eq. (A.5), which leads to:

$$\int_{\Omega} \psi \frac{\partial C_M}{\partial t} d\Omega + \int_{\Omega} \nabla \psi \cdot (D \nabla C_M) d\Omega - \oint_{\partial\Omega} \psi (D \nabla C_M) \cdot \mathbf{n} d\partial\Omega + \int_{\Omega} \psi \cdot \text{trap\_per\_free} \cdot \sum_{i=1}^3 \frac{\partial C_{T_i}}{\partial t} d\Omega = 0. \quad (\text{A.8})$$

Since no divergence terms exist in Eq. (A.6), no integration by parts is needed.

### A.5. Step 5: Derive the final weak form in inner product notation

Eqs. (A.6) and (A.8) can be expressed in inner product notation, where  $\langle a, b \rangle = \int_{\Omega} ab d\Omega$ .

Eq. (A.8) becomes

$$\langle \psi, \frac{\partial C_M}{\partial t} \rangle + \langle \nabla \psi, D \nabla C_M \rangle - \langle \psi, \text{trap\_per\_free} \cdot \sum_{i=1}^3 \frac{\partial C_{T_i}}{\partial t} \rangle + \oint_{\partial\Omega} \psi (D \nabla C_M) \cdot \mathbf{n} d\partial\Omega = 0, \quad (\text{A.9})$$

and, for  $i = 1, i = 2$ , and  $i = 3$ , Eq. (A.6) becomes

$$\langle \psi_i, \frac{\partial C_{T_i}}{\partial t} \rangle - \langle \psi_i, \alpha_i^i \frac{C_{T_i}^{\text{empty}} C_M}{N \cdot \text{trap\_per\_free}} \rangle + \langle \psi_i, \alpha_r^i C_{T_i} \rangle = 0. \quad (\text{A.10})$$

These weak forms of the equations can now be used for finite element analysis.

## Data availability

The TMAP8 code is open source and available at <https://github.com/idaholab/TMAP8>. It contains all the input files and python scripts used to generate the simulation results and figures in this manuscript. The complete TMAP8 documentation, including instructions on how to get started, the V&V cases described above, and descriptions of all of TMAP8's capabilities, is available at <https://mooseframework.inl.gov/TMAP8/index.html>.

Similarly, the multiphysics FENIX code is open source and available at <https://github.com/idaholab/FENIX>. The complete FENIX documentation, including instructions on how to get started, V&V and example cases, and descriptions of all of FENIX's capabilities, is available at <https://mooseframework.inl.gov/fenix/>.

## References

- [1] N. Taylor, B. Merrill, L. Cadwallader, L. Di Pace, L. El-Guebaly, P. Humrickhouse, D. Panayotov, T. Pinna, M.T. Porfiri, S. Reyes, M. Shimada, S. Willms, Materials-related issues in the safety and licensing of nuclear fusion facilities, Nucl. Fusion 57 (2017) 092003.
- [2] R.J. Pearson, A.B. Antoniazzi, W.J. Nuttall, Tritium supply and use: a key issue for the development of nuclear fusion energy, Fusion Eng. Des. 136 (2018) 1140–1148.
- [3] G.R. Longhurst, D.F. Holland, J.L. Jones, B.J. Merrill, TMAP4 User's Manual, Tech. Rep. EGG-FSP-10315, Idaho National Engineering Laboratory, 1992.

- [4] G.R. Longhurst, TMAP7 User Manual, Tech. Rep. INEEL/EXT-04-02352, Idaho National Engineering and Environmental Laboratory, 2008.
- [5] G.R. Longhurst, Tritium Behavior in ITER Beryllium, Tech. Rep. EGG-FSP-9304, Idaho National Engineering Laboratory, Idaho Falls, ID (USA), 1990.
- [6] G. Longhurst, S. Harms, E. Marwil, B. Miller, Verification and Validation of TMAP4, Tech. Rep. EGG-FSP-10347, Idaho National Engineering Laboratory, Idaho Falls, ID (United States), 1992.
- [7] J. Ambrosek, G. Longhurst, Verification and Validation of TMAP7, Tech. Rep. INEEL/EXT-04-01657, Idaho National Engineering and Environmental Laboratory, 2008.
- [8] J. Ambrosek, G.R. Longhurst, Verification and validation of the tritium transport code TMAP7, Fusion Sci. Technol. 48 (1) (2005) 468–471.
- [9] M.J. Baldwin, T. Schwarz-Selinger, J.H. Yu, R.P. Doerner, TMAP-7 simulation of D2 thermal release data from Be co-deposited layers, J. Nucl. Mater. 438 (2013) S967–S970.
- [10] A.D. Lindsay, C.T. Icenhour, P.-C.A. Simon, G. Singh, idaholab/TMAP8, 2021.
- [11] P.-C.A. Simon, P.W. Humrickhouse, A.D. Lindsay, Tritium transport modeling at the pore scale in ceramic breeder materials using TMAP8, IEEE Trans. Plasma Sci. (2022) 1–7.
- [12] M. Shimada, P.-C.A. Simon, C.T. Icenhour, G. Singh, Toward a high-fidelity tritium transport modeling for retention and permeation experiments, Fusion Eng. Des. 203 (2024) 114438.
- [13] G. Giudicelli, A. Lindsay, L. Harbour, C. Icenhour, M. Li, J.E. Hansel, P. German, P. Behne, O. Marin, R.H. Stogner, J.M. Miller, D. Schwen, Y. Wang, L. Munday, S. Schunert, B.W. Spencer, D. Yushu, A. Recuero, Z.M. Prince, M. Nezdur, T. Hu, Y. Miao, Y.S. Jung, C. Matthews, A. Novak, B. Langley, T. Truster, N. Nobre, B. Alger, D. Andrs, F. Kong, R. Carlsen, A.E. Slaughter, J.W. Peterson, D. Gaston, C. Permann, 3.0 - MOOSE: Enabling massively parallel multiphysics simulations, SoftwareX 26 (2024) 101690.
- [14] M. Eltawila, A.J. Novak, P.-C.A. Simon, G. Giudicelli, D. Gaston, Investigation of CAD-based geometry workflows for multiphysics fusion problems using OpenMC and MOOSE, in: Proceedings of the Pacific Basin Nuclear Conference, PBNC, American Nuclear Society, Idaho Falls, ID, 2024.
- [15] R. Williamson, J. Hales, S. Novascone, M. Tonks, D. Gaston, C. Permann, D. Andrs, R. Martineau, Multidimensional multiphysics simulation of nuclear fuel behavior, J. Nucl. Mater. 423 (1) (2012) 149–163.
- [16] M.R. Tonks, D. Gaston, P.C. Millett, D. Andrs, P. Talbot, An object-oriented finite element framework for multiphysics phase field simulations, Comput. Mater. Sci. 51 (1) (2012) 20–29.
- [17] D. Schwen, L.K. Aagesen, J.W. Peterson, M.R. Tonks, Rapid multiphase-field model development using a modular free energy based approach with automatic differentiation in MOOSE/MARMOT, Comput. Mater. Sci. 132 (2017) 36–45.
- [18] Z.M. Prince, J.T. Hanophy, V.M. Labouré, Y. Wang, L.H. Harbour, N. Choi, Neutron transport methods for multiphysics heterogeneous reactor core simulation in Griffin, Ann. Nucl. Energy 200 (2024) 110365.
- [19] A. Lindsay, G. Giudicelli, P. German, J. Peterson, Y. Wang, R. Freile, D. Andrs, P. Balestra, M. Tano, R. Hu, et al., Moose Navier–Stokes module, SoftwareX 23 (2023) 101503.
- [20] B.W. Spencer, W.M. Hoffman, S. Biswas, W. Jiang, A. Giorla, M.A. Backman, Grizzly and BlackBear: Structural component aging simulation codes, Nucl. Technol. 207 (2021) 981–1003.
- [21] A. Novak, D. Andrs, P. Shriwise, J. Fang, H. Yuan, D. Shaver, E. Merzari, P. Romano, R. Martineau, Coupled Monte Carlo and thermal-fluid modeling of high temperature gas reactors using Cardinal, Ann. Nucl. Energy 177 (2022) 109310.
- [22] C.T. Icenhour, A. Lindsay, S. Pitts, L. Aagesen, W. Jiang, idaholab/malamute, 2021.
- [23] R. Hu, T.H. Fanning, T. Sumner, Y. Yu, Status Report on NEAMS System Analysis Module Development, Tech. Rep., Argonne National Laboratory (ANL), Argonne, IL (United States), 2015.
- [24] P.-C.A. Simon, C.T. Icenhour, M. Shimada, A. Lindsay, G. Giudicelli, L. Harbour, D. Gaston, M.E. Tano, H. Brooks, A.J. Novak, M. Eltawila, A.M. Lietz, G. Gall, C. Fiorina, S. Reyes, Developing multiphysics, integrated, high-fidelity, massively parallel computational capabilities for fusion applications using MOOSE, in: Proceedings of the Pacific Basin Nuclear Conference 2024, American Nuclear Society, Idaho Falls, 2024, pp. 297–306.
- [25] F. Kong, P.W. Humrickhouse, Toward a fully integrated multiphysics simulation framework for fusion blanket design, IEEE Trans. Plasma Sci. (2022).
- [26] T. Franklin, C. Icenhour, P.-C.A. Simon, P. Humrickhouse, F. Kong, L. Carasik, New developments and verification of fusion blanket simulation capabilities in the MOOSE framework, Fusion Eng. Des. Submitt. (2024).
- [27] C.T. Icenhour, Fusion superconducting magnet electromagnetic modeling and simulation at idaho national laboratory: A review and look ahead, in: Proceedings of the Pacific Basin Nuclear Conference 2024, American Nuclear Society, Idaho Falls, 2024, pp. 307–316.
- [28] I. Ricapito, L. Candido, C. Moreno, A. Rueda, J. Serna, Tritium transport modelling in Europe: Current status, multi-physics integration and proposal of material property data, Fusion Eng. Des. 203 (2024) 114458.
- [29] R. Arredondo, K. Schmid, F. Subba, G.A. Spagnuolo, Preliminary estimates of tritium permeation and retention in the first wall of DEMO due to ion bombardment, Nucl. Mater. Energy 28 (2021) 101039.
- [30] R. Delaporte-Mathurin, J. Dark, G. Ferrero, E.A. Hodille, V. Kulagin, S. Meschini, FESTIM: An open-source code for hydrogen transport simulations, Int. J. Hydrog. Energy 63 (2024) 786–802.
- [31] E.A. Hodille, R. Delaporte-Mathurin, J. Denis, M. Pecovnik, E. Bernard, Y. Ferro, R. Sakamoto, Y. Charles, J. Mougnot, A.D. Backer, C.S. Becquart, S. Markelj, C. Grisolia, Modelling of hydrogen isotopes trapping, diffusion and permeation in divertor monoblocks under ITER-like conditions, Nucl. Fusion 61 (2021) 126003.
- [32] S. Dixon, aurora-multiphysics/achlys: Patch for latest moose version, 2023.
- [33] M. O’Neal, S.B. Seo, G.I. Maldonado, N.R. Brown, Assessment of BISON capabilities for component-level prediction of tritium transport in fusion and fission applications, Fusion Eng. Des. 175 (2022) 112996.
- [34] I.R. Cristescu, L. Dörr, A. Busigin, D. Murdoch, ITER dynamic tritium inventory modeling code, Fusion Sci. Technol. 48 (2005) 343–348.
- [35] L. Candido, C. Alberghi, Verification and validation of mHIT code over TMAP for hydrogen isotopes transport studies in fusion-relevant environments, Fusion Eng. Des. 172 (2021) 112740.
- [36] J.M. Nogués, J.A. Feliu, G. Campaña, E. Iraola, L. Batet, L. Sedano, Advanced tools for ITER tritium plant system modeling and design, Fusion Sci. Technol. (2020) 649–652.
- [37] A. Busigin, P. Gierszewski, CFTSIM-ITER dynamic fuel cycle model, Fusion Eng. Des. 39–40 (1998) 909–914.
- [38] A. Ying, M. Riva, M.Y. Ahn, C. Moreno, I. Cristescu, Recent advances in tritium modeling and its implications on tritium management for outer fuel cycle, Fusion Eng. Des. 161 (2020) 111895.
- [39] F. Franza, L.V. Boccacini, A. Ciampichetti, M. Zucchetti, Tritium transport analysis in HCPB DEMO blanket with the FUS-TPC code, Fusion Eng. Des. 88 (2013) 2444–2447.
- [40] T. Mui, R. Hu, Q. Zhou, T. Hua, System-level tritium transport modeling capability in SAM, in: Proceedings of ICAPP’24, American Nuclear Society, Las Vegas, Nevada, 2024.
- [41] M. Tonks, D. Gaston, C. Permann, P. Millett, G. Hansen, D. Wolf, A coupling methodology for mesoscale-informed nuclear fuel performance codes, Nucl. Eng. Des. 240 (2010) 2877–2883.
- [42] P.C.A. Simon, J.H. Ke, C. Jiang, L.K. Aagesen, W. Jiang, Multiscale, mechanistic modeling of irradiation-enhanced silver diffusion in TRISO particles, J. Nucl. Mater. 603 (2025) 155464.
- [43] P.-C.A. Simon, C.T. Icenhour, M. Shimada, G. Giudicelli, L. Harbour, D. Gaston, A.J. Novak, M. Eltawila, A.M. Lietz, G. Gall, idaholab/FENIX, 2024.
- [44] A.E. Slaughter, Z.M. Prince, P. German, I. Halvic, W. Jiang, B.W. Spencer, S.L.N. Dhulipala, D.R. Gaston, MOOSE stochastic tools: A module for performing parallel, memory-efficient in situ stochastic simulations, SoftwareX 22 (2023) 101345.
- [45] J. Fish, T. Belytschko, A First Course in Finite Elements, Wiley, 2007.
- [46] L.E. Schwer, An overview of the PTC 60V&V 10: guide for verification and validation in computational solid mechanics, Eng. Comput. 23 (4) (2007) 245–252.
- [47] A.E. Slaughter, C.J. Permann, J.M. Miller, B.K. Alger, S.R. Novascone, Continuous integration, in-code documentation, and automation for nuclear quality assurance conformance, Nucl. Technol. 207 (7) (2021) 923–930.
- [48] American Society of Mechanical Engineers, ASME NQA-1-2008 with the NQA-1a-2009 Addenda: Quality Assurance Requirements for Nuclear Facility Applications, first ed., American Society of Mechanical Engineers, 2009.
- [49] B. Collin, R. Gardner, M.J. Hackett, R. Latta, R.C. Gallagher, T. Gerczak, A. Le Coq, K. Linton, TRISO fuel performance pre-test predictions of HFIR MiniFuel high power irradiation, Trans. Am. Nucl. Soc. 126 (1) (2022) 404–407.
- [50] KP-FHR Team, KP-FHR Fuel Performance Methodology, Technical Report KP-TR-010-NP, Revision 3, Kairos Power LLC, Alameda, CA, USA, 2021.
- [51] T.J.R. Hughes, The Finite Element Method: Linear Static and Dynamic Finite Element Analysis, Dover Publications, Mineola, New York, 2000.
- [52] M.S. Gockenbach, Understanding and Implementing the Finite Element Method, Society for Industrial and Applied Mathematics, Philadelphia, PA, 2006.
- [53] H.S. Carslaw, J.C. Jaeger, Conduction of Heat in Solids, second ed., Oxford University Press, 1959.
- [54] C. DeChant, C. Icenhour, S. Keniley, G. Gall, A. Lindsay, D. Curreli, S. Shannon, Verification and validation of the open-source plasma fluid code: Zapdos, Comput. Phys. Comm. 291 (2023) 108837.
- [55] R. Delaporte-Mathurin, E.A. Hodille, J. Mougnot, Y. Charles, C. Grisolia, Finite element analysis of hydrogen retention in ITER plasma facing components using FESTIM, Nucl. Mater. Energy 21 (2019) 100709.
- [56] Y.-C. Li, P.J. Cleall, Analytical solutions for contaminant diffusion in double-layered porous media, J. Geotech. Geoenviron. Eng. 136 (11) (2010) 1542–1554.
- [57] F.P. Incropera, D.P. DeWitt, Fundamentals of Heat and Mass Transfer, fifth ed., John Wiley & Sons, New York, 2002.
- [58] R. Anderl, D. Holland, D. Struttman, G. Longhurst, B. Merrill, Tritium Permeation in Stainless-Steel Structures Exposed to Plasma Ions, Tech. Rep., Idaho National Engineering Lab., Idaho Falls (USA), 1985.

- [59] J. Biersack, J. Ziegler, The stopping and range of ions in solids, in: *Ion Implantation Techniques: Lectures Given At the Ion Implantation School in Connection with Fourth International Conference on Ion Implantation: Equipment and Techniques* Berchtesgaden, Fed. Rep. of Germany, Springer, 1982, pp. 122–156.
- [60] R. Macaulay-Newcombe, D. Thompson, W. Smeltzer, Deuterium diffusion, trapping and release in ion-implanted beryllium, *Fusion Eng. Des.* 18 (1991) 419–424.
- [61] K. Wilson, R. Causey, W. Hsu, B. Mills, M. Smith, J. Whitley, Beryllium—a better tokamak plasma-facing material? *J. Vac. Sci. Technol. A: Vac. Surfaces, Films* 8 (3) (1990) 1750–1759.
- [62] W.A. Swansiger, Summary abstract: Tritium solubility in high purity beryllium, *J. Vac. Sci. Technol. A* 4 (1986) 1216–1217.
- [63] E. Abramov, M. Riehm, D. Thompson, W. Smeltzer, Deuterium permeation and diffusion in high-purity beryllium, *J. Nucl. Mater.* 175 (1–2) (1990) 90–95.
- [64] D.L. Baldwin, O.D. Slagle, D.S. Gelles, Tritium release from irradiated beryllium at elevated temperatures, *J. Nucl. Mater.* 179–181 (1991) 329–334.
- [65] R. Macaulay-Newcombe, D. Thompson, W. Smeltzer, Thermal absorption and desorption of deuterium in beryllium and beryllium oxide, *J. Nucl. Mater.* 191 (1992) 263–267.
- [66] J. Fowler, D. Chandra, T. Elleman, A. Payne, K. Verghese, Tritium diffusion in Al<sub>2</sub>O<sub>3</sub> and BeO, *J. Am. Ceram. Soc.* 60 (3–4) (1977) 155–161.
- [67] S.K. Au, J.L. Beck, Estimation of small failure probabilities in high dimensions by subset simulation, *Probabilistic Eng. Mech.* 16 (4) (2001) 263–277.
- [68] S.L. Dhulipala, M.D. Shields, P. Chakroborty, W. Jiang, B.W. Spencer, J.D. Hales, V.M. Laboure, Z.M. Prince, C. Bolisetti, Y. Che, Reliability estimation of an advanced nuclear fuel using coupled active learning, multifidelity modeling, and subset simulation, *Reliab. Eng. Syst. Saf.* 226 (2022) 108693.
- [69] D.F. Holland, R.A. Jalbert, A model for tritium concentration following tritium release into a test cell and subsequent operation of an atmospheric cleanup system, in: *Eleventh Symposium on Fusion Engineering*, Vol. 1, IEEE Cat. No. CH2251-7, Austin, TX, 1986.
- [70] M. Abdou, M. Riva, A. Ying, C. Day, A. Loarte, L.R. Baylor, P. Humrickhouse, T.F. Fuerst, S. Cho, Physics and technology considerations for the deuterium–tritium fuel cycle and conditions for tritium fuel self sufficiency, *Nucl. Fusion* 61 (1) (2021) 013001.